JCB Journal of Cell Biology

ARTICLE

A membrane-sensing mechanism links lipid metabolism to protein degradation at the nuclear envelope

Shoken Lee[1], Jake W. Carrasquillo Rodríguez[1], Holly Merta[1], and Shirin Bahmanyar[1]

Lipid composition determines organelle identity; however, whether the lipid composition of the inner nuclear membrane (INM) domain of the ER contributes to its identity is not known. Here, we show that the INM lipid environment of animal cells is under local control by CTDNEP1, the master regulator of the phosphatidic acid phosphatase lipin 1. Loss of CTDNEP1 reduces association of an INM-specific diacylglycerol (DAG) biosensor and results in a decreased percentage of polyunsaturated containing DAG species. Alterations in DAG metabolism impact the levels of the resident INM protein Sun2, which is under local proteasomal regulation. We identify a lipid-binding amphipathic helix (AH) in the nucleoplasmic domain of Sun2 that prefers membrane packing defects. INM dissociation of the Sun2 AH is linked to its proteasomal degradation. We suggest that direct lipid–protein interactions contribute to sculpting the INM proteome and that INM identity is adaptable to lipid metabolism, which has broad implications on disease mechanisms associated with the nuclear envelope.

Introduction

The nuclear envelope (NE) is a highly specialized domain of the ER (Baumann and Walz, 2001; Hetzer, 2010). The NE is made up of the inner nuclear membrane (INM) that faces chromatin and is adjoined with the outer nuclear membrane (ONM), which is directly continuous with the perinuclear ER. Nuclear pore complexes (NPCs) reside at fusion points between the INM and ONM to direct the bidirectional traffic of macromolecules across the NE (Hampoelz et al., 2019; Lin and Hoelz, 2019). The segregation of the INM from the cytoplasm provides a confined environment for the NE to carry out its unique functions, which include nucleo-cytoskeletal coupling, genome organization, and lipid metabolism (Bahmanyar and Schlieker, 2020; Starr and Fridolfsson, 2010; Ungricht and Kutay, 2017). How the NE gains its unique structure and identity within the ER is not fully understood.

In metazoans, the intermediate filament lamin proteins form a meshwork at the nuclear face of the INM to provide mechanical stability to the NE (Dechat et al., 2010; Dechat et al., 2008). A subset of integral membrane proteins diffuse from their site of synthesis on ribosome-bound ER sheets to the INM where they selectively concentrate through interactions with chromatin and the nuclear lamina (Boni et al., 2015; Katta et al., 2014; Ungricht et al., 2015). Evidence also suggests that protein degradation and trafficking monitor and refine the INM proteome (Buchwalter et al., 2019; Foresti et al., 2014; Khmelinskii et al., 2014; Krshnan et al., 2022a; Natarajan et al., 2020). Mutations in nuclear lamins and INM proteins give rise to a diverse array of human disorders, further highlighting the importance of INM functions in cellular and human physiology (Shin and Worman, 2022).

Direct protein binding to a unique INM lipid environment (e.g., lipids with specific head groups or lipid packing density) could provide a way to enrich and remodel the INM proteome. In the vesicular trafficking pathway, the unique bilayer lipid composition of membrane-bound compartments confers organelle identity by recruiting proteins with specific lipid-binding domains (Behnia and Munro, 2005). While direct lipid-binding regions in resident INM proteins have not been identified, some proteins associated with nuclear pore biogenesis and quality control contain amphipathic helices (Cornell, 2016; Haider et al., 2018; Mészáros et al., 2015; Thaller et al., 2021; Vollmer et al., 2015). Amphipathic helixes (AHs) fold when inserted into the polar–non-polar interface of lipid bilayers that contain packing defects. AHs can also serve to destabilize bilayer lipids for membrane remodeling or stabilize membranes under lipid stress. Some AHs sense membrane

---

[1]Department of Molecular Cellular and Developmental Biology, Yale University, New Haven, CT, USA.

Correspondence to Shirin Bahmanyar: shirin.bahmanyar@yale.edu.

Rockefeller University Press
J. Cell Biol. 2023 Vol. 222 No. 9 e202304026
https://doi.org/10.1083/jcb.202304026

curvature or, in rare cases, specific lipids (Drin and Antonny, 2010; Giménez-Andrés et al., 2018; Hofbauer et al., 2018). Thus, the existence of AHs in INM proteins would be one way to selectively concentrate proteins at the INM and simultaneously facilitate sensitivity to lipid metabolism.

In the absence of active restriction mechanisms, lipid chemistries between the INM and peripheral ER would equilibrate because of free lipid diffusion. Key findings in budding yeast and mammalian cells revealed that INM lipids are dynamically altered in response to lipid metabolism (Barbosa et al., 2019; Foo et al., 2023; Haider et al., 2018; Romanauska and Köhler, 2018; Romanauska and Köhler, 2021; Sołtysik et al., 2021; Tsuji et al., 2019). In budding yeast, protein biosensors appended to nuclear localization signals (NLSs) revealed enrichment of diacylglycerol (DAG) at the INM at a steady state (Romanauska and Köhler, 2018). Protein biosensors that detect the steady state content of INM lipids in mammalian cells had not been developed.

One way to generate lipid asymmetry is through the continuous turnover of specific lipids at the INM through the enrichment of certain lipid enzymes or their regulators (Bahmanyar and Schlieker, 2020). There is evidence in metazoans that enzymes involved in lipid metabolism can reach the INM (Sołtysik et al., 2021). In *Caenorhabditis elegans* and *Drosophila*, the master regulator of the phosphatidic acid phosphatase, lipin (CNEP-1 in *C. elegans* and CTDNEP1 in humans), is enriched at the NE (Bahmanyar et al., 2014; Jacquemyn et al., 2021), providing a way to generate high concentrations of DAG in one location (e.g., INM) relative to the other (e.g., peripheral ER).

Here, we establish a nuclear targeted, genetically encoded fluorescent protein biosensor for DAG that associates with the INM at steady state in mammalian cells (hereafter termed "INM-DAG sensor"). We show that CTDNEP1 and its binding partner NEP1R1 can reach the INM, providing a way to maintain relatively high levels of DAG at and in proximity to the INM. Lipidomics analysis of CTDNEP1 KO cells revealed a decrease in the percentage of DAG species with polyunsaturated long-chain fatty acids, which are known to induce packing defects in membranes and serve as precursors to signaling molecules at the INM (Harayama and Shimizu, 2020; Lomakin et al., 2020; Venturini et al., 2020). We identify a lipid-binding AH in the nucleoplasmic domain of the resident INM protein Sun2 that prefers membrane packing defects in vitro. Retention of Sun2 at the NE involves the membrane sensing capability of its AH and is linked to its proteasomal degradation (Ji et al., 2022; Kim et al., 2015; Krshnan et al., 2022a; Loveless et al., 2015), which we demonstrate happens locally at the INM. Together, our data show that a resident NE protein contains a membrane-binding AH that associates with the unique INM lipid environment and contributes to its INM retention. These results suggest that the unique lipid chemistry of the INM contributes to its protein identity and that the NE is adaptable to lipid metabolism, which has important implications for the many functions of the NE, including genome regulation and protection.

Results

Local control the INM lipid environment revealed by an INM-DAG sensor

Lipid metabolism occurs locally at the INM (Barbosa et al., 2019; Haider et al., 2018; Romanauska and Köhler, 2018; Romanauska and Köhler, 2021; Sołtysik et al., 2021; Tsuji et al., 2019), but mechanisms that control the bilayer lipid content of the INM at steady state are not fully understood. We chose to focus on the NE-enriched protein phosphatase CTDNEP1 because of its known role in regulating the Mg^{2+}-dependent phosphatidic acid phosphatase (PAP), lipin 1 (Fig. 1 A; Han et al., 2012; Kim et al., 2007; Merta et al., 2021). Lipin 1 is mostly soluble at steady state and localizes to both the nucleus and cytoplasm (Merta et al., 2021; Peterson et al., 2011). We used CRISPR-Cas9 genome editing to endogenously tag human CTDNEP1 with EGFP at the endogenous locus (CTDNEP1^EGFP; Fig. 1 B). CTDNEP1^EGFP localized in a punctate pattern at the NE in U2OS cells, as well as to other cytoplasmic membrane structures that likely represent an ER-associated pool of the endogenous protein (Fig. 1 B). CTDNEP1^EGFP puncta at the nuclear rim mostly intercalated with NPCs, as marked by POM121-mCherry (Fig. 1 B, inset). The split-sfCherry2 system (Feng et al., 2017), in which a piece of $sfCherry_{1-10}$ is fused to either CTDNEP1 or NEP1R1, was co-transfected with $sfCherry_{11}$ fused to Histone-2B and revealed the population of CTDNEP1 and NEP1R1 that can reach the INM (Fig. S1 A). Localization of both CTDNEP1 and NEP1R1 to the INM suggested that the local lipid environment, and particularly PA/DAG metabolism, in animal cells may be controlled through regulation of lipin 1.

CTDNEP1 maintains a stable and dephosphorylated pool of lipin 1 in the nucleus and so a decrease in the levels of DAG at the INM would be a predicted outcome of loss of CTDNEP1. Our prior whole-cell pooled analysis of DAG and phosphatidic acid (PA) in CRISPR-Cas9 edited CTDNEP1 knockout (KO) cells (Merta et al., 2021) did not detect changes in their absolute levels (Merta et al., 2021). We conducted lipidomics analysis on DAG species (e.g., saturated versus unsaturated) to account for differences in fatty acyl chain composition that would be missed from the pooled analysis. The percentage of DAG relative to total cellular lipid levels is unchanged in CTDNEP1 KO cells (Fig. 1 C), consistent with our prior analysis (Merta et al., 2021). Instead, there is an increase in the percentage of DAG species that contain saturated and/or mono-unsaturated acyl chains (e.g., 16:0/16:0 and 16:0/18:1; Fig. 1 C and Fig. S1 B). This is directly in line with our prior work showing increased FA synthesis in these cells that feeds into lipid synthesis and the compensatory increase in the activity of Mg^{2+}-independent PAPs that function at cytosolic organelles (Merta et al., 2021).

The percentages of DAG species containing long-chain polyunsaturated fatty acid (PUFAs; e.g., 20:4, 22:4, 20:3), which induce packing defects in membranes and are involved in INM lipid signaling (Harayama and Shimizu, 2020; Lomakin et al., 2020; Venturini et al., 2020), were decreased in CTDNEP1 KO cells (Fig. 1 C and Fig. S1 B). Thus, specific species of DAG with PUFAs may be directly regulated by the CTDNEP1/lipin pathway at the INM; however, technical challenges of isolating the INM

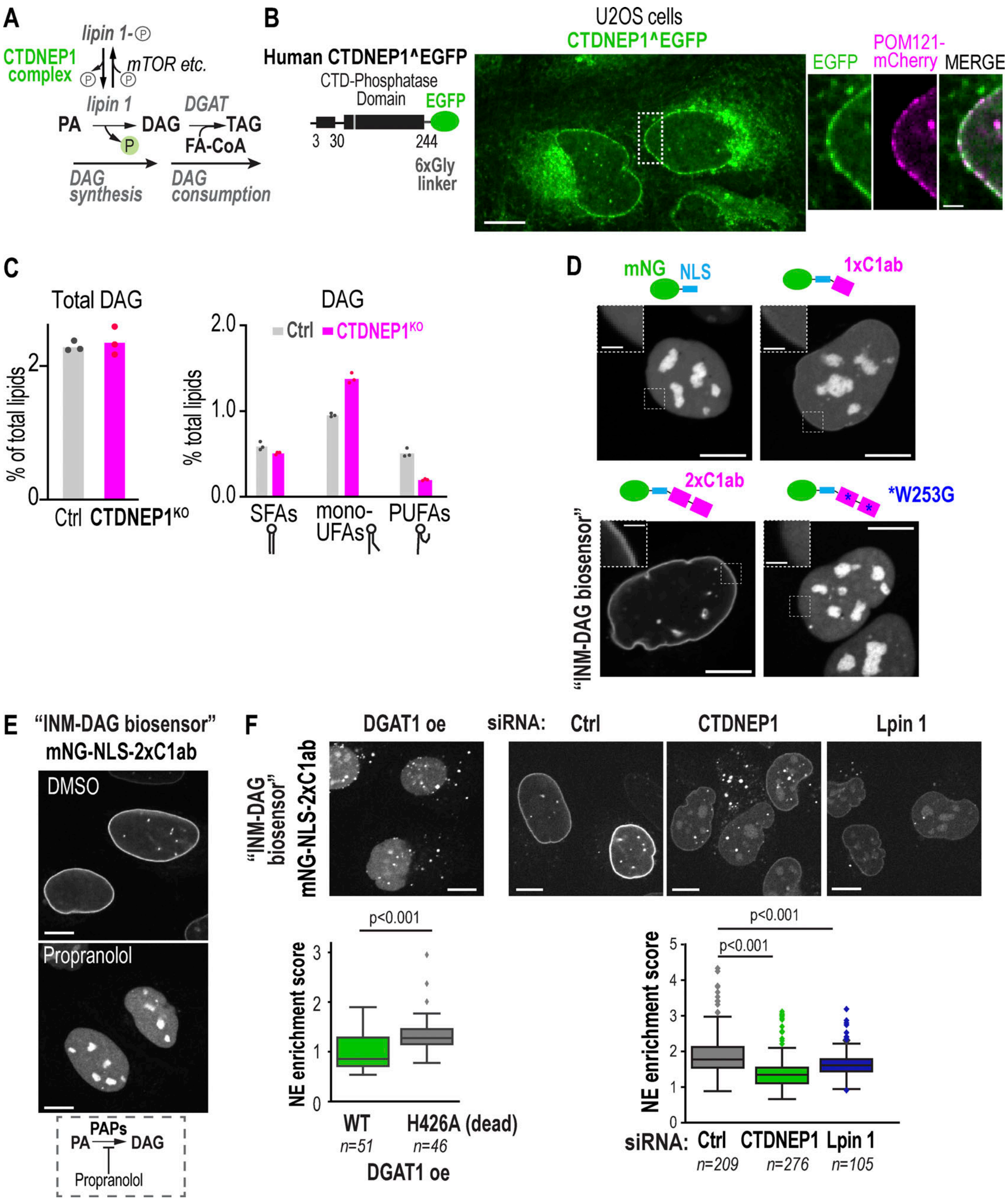

Figure 1. **A genetically encoded biosensor for the INM lipid environment is sensitive to DAG metabolism. (A)** Schematic representation of CTDNEP1, lipin 1, and DGAT in relation to production and consumption of diacylglycerol (DAG). **(B)** Spinning disk confocal images of CTDNEP1^EGFP in live U2OS cells. Insets show co-localization with the NPC marker POM121-mCherry. **(C)** Mol% of lipids analyzed by mass spectrometry. Saturated fatty acid (SFA): DAG with only SFA chains; mono-unsaturated fatty acid (mono-UFA): DAG with at least one mono-UFA chain but without PUFA; PUFA: DAG with at least one PUFA chain. Each dot represents a technical replicate. **(D)** Spinning disk confocal images of live U2OS cells expressing the indicated DAG biosensors. Insets show nuclear rim. **(E)** Spinning disk confocal images of live U2OS cells stably expressing mNG-NLS-2xC1b (aka "INM-DAG biosensor") and treated with propranolol to inhibit all phosphatidic acid phosphatases. **(F)** Spinning disk confocal images of live U2OS cells stably expressing the INM-DAG biosensor and transiently expressed with mScarlet-DGAT1 or treated with indicated siRNAs. Box plot: NE enrichment scores (internally normalized fluorescence intensity values—see Fig. S1 C) pooled from 2 to 4 independent experiments. *n* indicates the number of cells quantified. P values: Tukey HSD test. Scale bars: 2 µm in insets in B and D and 10 µm in others.

from the rest of the ER for biochemical lipid analysis precludes directly determining the specific lipid make-up of the INM.

To bypass the need for biochemical lipid analysis of the INM, we developed a fluorescent-tagged genetically encoded protein biosensor of DAG as a readout of the INM lipid environment. We utilized the C1a-C1b (hereafter C1ab) domains of protein kinase C theta, which was used for detecting DAG at other organelles (Carrasco and Merida, 2004; Spitaler et al., 2006) and prefers binding to PUFA-containing DAG species (Carrasco and Merida, 2004). A single C1ab domain appended to an NLS (1xC1ab) showed faint localization at the nuclear rim, whereas a tandem repeat of the C1ab domains (2xC1ab) fused to an NLS and to mNeonGreen (mNG; hereafter referred to as "INM-DAG biosensor") showed clear nuclear rim localization with intranuclear localization that resembles nucleoplasmic reticulum (Fig. 1 D). The INM-DAG biosensor with its key residue for DAG binding mutated (W253G; Das and Rahman, 2014; Rahman et al., 2013) localized to the nucleoplasm and nuclear bodies in a non-specific manner that was indistinguishable from localization of mNG-NLS (Fig. 1 D). Thus, the DAG binding capacity of the INM-DAG biosensor facilitates its association with the INM.

Inner nuclear membrane localization of the INM-DAG biosensor is sensitive to manipulations of DAG metabolism. Localization of the INM-DAG biosensor to the nuclear rim was abolished after 5 min in cells treated with a small molecule inhibitor of Mg^{2+}-dependent and -independent PA phosphatases (propranolol; Fig. 1 E), which has been shown to deplete DAG from cytosolic organelle membranes (Baron and Malhotra, 2002; Carrasco and Merida, 2004). RNAi-mediated depletion of CTDNEP1 or lipin 1, as well as overexpression of wild-type but not catalytically inactive mutant DGAT1 to consume DAG (McFie et al., 2010), reduced INM-DAG biosensor association with the INM (Fig. 1 F), albeit to a lesser extent than short-term propranolol treatment. Redistribution of the biosensor to the nucleoplasm and nucleoli as well as accumulation of the biosensor in ectopic punctate structures that likely represent aggregated protein resulted from reduced binding sites at the INM. The reduced levels of the INM-DAG biosensor at the nuclear rim under these conditions were confirmed in an unbiased manner using semiautomated image analysis to determine the ratio of the fluorescent signal of the INM-DAG biosensor at the nuclear rim and nucleoplasm ("NE enrichment score"; Fig. S1 C and Fig. 1 F). The evidence that CTDNEP1 functions at the NE as well as the evidence for TAG synthesis occurring at the INM by DGAT1 (Sołtysik et al., 2021) support the possibility that lipid metabolism occurs directly at the INM of animal cells to impact the INM lipid environment. However, DGAT1 and lipin 1 also function at the ER and so we can not exclude the possibility that lipid equilibration between the ER and INM impacts the INM lipid composition under these conditions.

Protein levels of the nucleo-cytoskeletal linker Sun2 are sensitive to lipid metabolism

Whether resident INM proteins are regulated by metabolic changes in bilayer lipids is not known. Prior work has shown that the levels of the resident INM protein Sun2 depend on CTDNEP1 and casein kinase 2 (Krshnan et al., 2022a). We set out to test if alterations in lipid metabolism resulting from loss of CTDNEP1 contribute to the regulation of Sun2 protein levels. Sun proteins are a family of nucleo-cytoskeletal linkers defined by a luminal SUN domain at their C-terminus that facilitates binding to the cytoskeleton through direct association with KASH proteins in the ONM (Chang et al., 2015). Sun1 and Sun2 are ubiquitously expressed, and recent studies indicate that Sun2 has cellular- and tissue-level functions distinct from Sun1 (Belaadi et al., 2022; Luxton et al., 2010; Stewart et al., 2019; Stewart et al., 2015; Zhu et al., 2017).

Comparing endogenous nuclear rim localization of five other INM proteins in control U2OS and CTDNEP1 KO cells (Merta et al., 2021) showed a selective reduction in fluorescence signal specific to Sun2 (Fig. 2 A and Fig. S2 A). Reduction of global protein levels of Sun2 but not Sun1 resulting from deletion of CTDNEP1 was further supported by immunoblot analysis (Fig. 2 B and Fig. S2 B). CTDNEP1 KO, but not RNAi-depleted, cells contained higher levels of Sun1 protein, perhaps because of long-term compensatory mechanisms (Fig. 2 B and Fig. S2 B). Sun2 levels were restored upon expression of wild-type CTDNEP1 (CTDNEP1-mAID-HA), but not the phosphatase dead mutant (phosphatase-dead, PD; Fig. 2 C; Merta et al., 2021). The global reduction of Sun2 protein was not due to changes in transcript levels in CTDNEP1 KO cells (Fig. S2 C) and could not be explained by loss of association of Sun2 with CTDNEP1 because neither wild-type nor phosphatase dead (PD) CTDNEP1 co-immunoprecipitates with Sun2 (Fig. S2 D). The selective loss of Sun2 protein levels does not result from global upregulation of de novo lipid synthesis in CTDNEP1 KO cells because the nuclear rim localization of Sun2 was unaffected in cells treated with TOFA, a small molecule inhibitor of the rate-limiting enzyme in de novo fatty-acid synthesis that restores ER expansion resulting from loss of CTDNEP1 (Fig. S2 E; Merta et al., 2021). We did not observe a reduction of emerin in CTDNEP1 KO cells (Fig. S2 B), which has been shown to be downregulated along with Sun2 upon disruption of ER homeostasis (Buchwalter et al., 2019). Sun2 associates with nuclear lamins (Chang et al., 2015), and lamin A knockdown lowered Sun2 levels (Fig. 2 B). However, we did not observe a change in lamin A/C levels upon loss of CTDNEP1 or lipin 1 (Fig. 2 B), and lamin A knockdown impacted both Sun2 and Sun1 localization (Fig. S2, F and G).

Sun2, but not Sun1, is targeted for degradation by the proteasome (Ji et al., 2022; Kim et al., 2015; Krshnan et al., 2022a; Loveless et al., 2015), which is mediated by the substrate recognition subunit of the $SCF^{b\text{-}trcp}$ proteins β-TrCP1/Fbxw1 and β-Trcp2/Fbx11 (Kim et al., 2015; Krshnan et al., 2022a; Loveless et al., 2015). Sun2 levels were partially restored in CTDNEP1 KO cells treated with MLN4924, in which the $SCF^{b\text{-}trcp}$ function was inhibited, or with RNAi-depletion of $SCF^{b\text{-}trcp}$ subunits (Fig. S2 H), confirming that Sun2 protein is under proteasomal regulation.

Transient overexpression of RNAi-resistant wild-type human lipin 1, but not the catalytically inactive mutant, partially restored localization of Sun2 at the nuclear rim in CTDNEP1 KO cells RNAi-depleted of endogenous lipin 1, as shown by blind categorization (Fig. 2 D) and unbiased automated image analysis (Fig. S2 I). Additionally, RNAi-depletion of lipin 1 after 72 h showed a reduction in global Sun2 protein levels (Fig. 2 B) concomitant with a loss of Sun2 at the nuclear rim in ~30% of cells (Fig. S2 F). A significant proportion of cells overexpressing wild-type but not catalytically inactive DGAT1 or DGAT2 (McFie et al., 2010; Stone et al., 2006) also showed selective loss of Sun2, but not Sun1, at the nuclear rim (Fig. 2 E and Fig. S2 J). Thus, alterations in lipid enzymes involved in the synthesis and consumption of DAG impact the levels of Sun2 at the nuclear rim. The less pronounced effects of lipin 1 compared with CTDNEP1 on Sun2 protein levels suggest that CTDNEP1 may be involved in aspects of Sun2 regulation that are

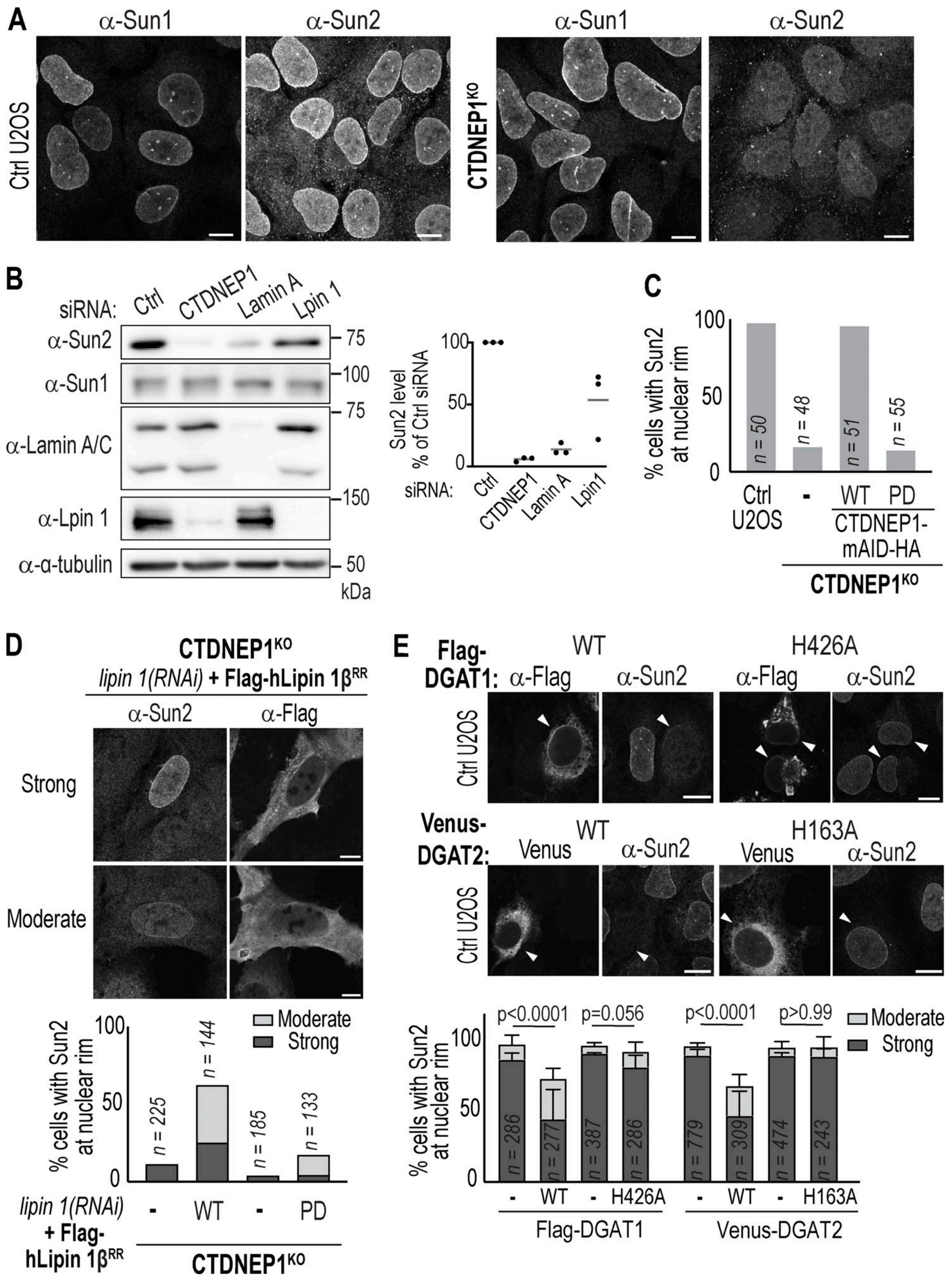

Figure 2. **Sun2 localization and protein levels are sensitive to lipid metabolism.** **(A)** Confocal images of U2OS control and CTDNEP1 KO cells immunostained with antibodies against indicated proteins. **(B)** Immunoblot of cell lysates from control U2OS cells treated with indicated siRNAs. Right: Plot of quantification of relative Sun2 band intensities normalized to tubulin under indicated conditions as percentage of control. Each dot indicates an independent experiment. **(C)** Plot of quantification of Sun2 localization at nuclear rim in indicated conditions. *n* indicates the number of cells quantified. **(D)** Representative images of immunostained CTDNEP1 KO cells showing different categories of Sun2 localization at nuclear rim and plot of blind quantification under indicated conditions. *n* indicates the number of cells quantified pooled from two independent experiments. **(E)** Confocal images of immunostained U2OS cells expressing indicated constructs. Plot shows blind quantification of Sun2 localization at nuclear rim. *n* indicates the number of cells quantified. P values: Fisher's exact test (moderate vs. others) with *N* = 3 independent experiments (mean + SD is shown). All scale bars: 10 μm. Source data are available for this figure: SourceData F2.

not solely through lipin 1. Taken together, these results suggest that lipid metabolism influences the nuclear rim localization of Sun2 and its protein levels.

Sun2 contains a membrane-sensing amphipathic helix

We hypothesized that direct membrane binding by Sun2 may be linked to its regulation. Sun1 and Sun2 both contain an N-terminal nucleoplasmic (NP) domain that includes hydrophobic alpha helices (Liu et al., 2007; Majumder et al., 2018; Turgay et al., 2010), followed by a transmembrane helix (or helices in Sun1 [Majumder et al., 2018]), a large luminal domain made up of coiled-coils that oligomerize, and a C-terminal SUN-domain that associates with short peptides in KASH domain proteins that span the outer nuclear membrane (Sosa et al., 2012). Neither the classical NLS (aa 33–55) nor ER-retrieval signal (aa 102–105) in the Sun2 NP domain is necessary on its own for the localization of full-length Sun2 at the INM (Turgay et al., 2010). We focused on a hydrophobic predicted alpha helix in the NP domain that had not been systematically tested for its role in INM retention of Sun2. In silico analysis predicted the presence of an amphipathic helix (AH) in Sun2 residues 155–180 (Fig. 3 A). The known preference of AHs for packing defects in membrane bilayers, which occur with local enrichment of cone-shaped lipids, such as DAG, and mono- or polyunsaturated fatty acids (Drin and Antonny, 2010; Vamparys et al., 2013; Vanni et al., 2014), led us to further explore if the predicted AH of Sun2 associates with the INM.

The predicted AH of Sun2 binds directly to lipid bilayers in vitro. A Sun2 AH peptide (residues 151–180) purified from *Escherichia coli* as a GST fusion binds to liposomes generated from unsaturated fatty acids (palmitoyl-oleoyl-phosphatidylcholine or POPC; 16:0/18:1; Fig. 3, B and C), indicating that this portion of Sun2 binds membranes directly. There was a decrease in binding of the AH of Sun2 to liposomes generated with saturated acyl chains (dipalmitoyl-PC, DPPC; 16:0/16:0) or cholesterol (80% POPC + 20% cholesterol) that contain less lipid packing defects (Fig. 3, B and C; and Fig. S3 A). While the majority of the in vitro purified GST-AH(Sun2) associates with liposomes formed from unsaturated phospholipids (Fig. 3, B and C; and Fig. S3 B; dioleoyl-PC or DOPC; 18:1/18:1 and dioleoyl-PE or DOPE; 18:1/18:1), there was a slight increase in the liposome binding fraction when DAG (dioleoyl-DAG; 18:1/18:1) was included (Fig. 3 C and Fig. S3 B). Importantly, mutating 6 of the 11 bulky hydrophobic residues in the AH to alanine (hereafter LVW/A mutant; Fig. 3 A) completely abolished its liposome-binding capability in vitro showing that the bulky hydrophobic residues of this segment are important for membrane association (Fig. 3 C and Fig. S3 C). We conclude that Sun2 contains an AH that binds lipid bilayers with a preference for membrane packing defects (rather than the concentrations of specific lipid species), which may represent bulk membrane properties present at the INM.

The AH of Sun2 was sufficient to target the ER when expressed from a plasmid as an mNG fusion in control U2OS cells (Fig. 3 D). Selective permeabilization of the plasma membrane, but not internal membranes, by digitonin (Adam et al., 1990) followed by antibody staining against the N-terminal HA- and C-terminal mNG tags appended to residues 151–180 of Sun2 demonstrated that the AH does not cross the membrane bilayer (Fig. S3 D). The Sun2-AH appended with an NLS (hereafter AH-mNG-NLS) strongly enriched at the INM in control U2OS cells (Fig. 3 D), whereas the mutant AH defective in membrane binding (AH[LVW/A]-mNG-NLS) localized to the nucleoplasm (Fig. 3 D). Together, these data indicate that the Sun2 AH is a peripheral ER/NE membrane binding protein segment that when targeted to the nucleus preferentially binds to the INM through its bulky hydrophobic residues. Thus, the INM likely contains regions with packing defects that are favorable for binding by the Sun2 AH.

Localization of the membrane-binding AH of Sun2 to the nuclear rim is sensitive to alterations in DAG metabolism. Propranolol treatment to inhibit all PAPs displaced AH-mNG-NLS from the nuclear rim to the nucleoplasm in control cells (Fig. 3 E). The Sun2 AH-mNG-NLS was partially mistargeted to the ER in CTDNEP1 KO cells (Fig. 3 F). Nuclear rim association of Sun2 AH-mNG-NLS in CTDNEP1 KO cells was restored by overexpression of wild-type, but not phosphatase dead CTDNEP1 (Fig. S3 E). Importantly, overexpression of wild-type lipin 1, but not the phosphatase inactive mutant, in CTDNEP1 KO cells suppressed the ER mislocalization of the Sun2 AH-mNG-NLS (Fig. 3 G) indicating that altered lipid metabolism underlies reduced INM retention of the Sun2 AH in these cells.

Furthemore, the dispersal of the Sun2 AH-mNG-NLS to the ER in CTDNEP1 KO cells does not result from ER expansion or other secondary defects on nuclear integrity and is specific to Sun2. CTDNEP1 KO cells treated with TOFA to recover ER morphology did not restore ER mislocalization of AH-mNG-NLS (Fig. S3 E). Loss of CTDNEP1 did not impact nuclear retention of a soluble mNG-NLS reporter (Fig. S3 F) nor a peptide with a predicted AH in Sun1 fused to an NLS that targets both to the nucleoplasm and nuclear rim (Fig. S3 G). The mislocalization to the ER, rather than to the nucleoplasm, suggested that the Sun2 AH may be weakly retained at the INM in CTDNEP1 KO cells. Under these conditions, the NLS is unable to override the membrane binding capacity of the AH resulting in its association with ER membranes rather than accumulation in the nucleoplasm. Together, these results indicate that the INM lipid environment, which is maintained by the CTDNEP1/lipin 1 pathway, contributes to NE retention of the Sun2 AH through direct membrane binding.

We generated a series of chimeras between Sun1 and Sun2 to determine the selective sensitivity of the Sun2 AH to loss of CTDNEP1. All chimeras were expressed at either lower or similar levels in control and CTDNEP1 KO cells when transiently expressed (Fig. S4 A). Exogenously overexpressed Sun2-mNG, but not Sun1-mNG, resulted in reduced NE enrichment and increased ER mislocalization in CTDNEP1 KO cells (Fig. S4 B) confirming that a unique feature in Sun2, that is not present in Sun1, may be responsive to metabolic changes in INM lipids resulting from loss of CTDNEP1.

We hypothesized that the AH sequence of Sun2 in combination with other nucleoplasmic or luminal element(s) helps to retain Sun2 at the INM. Prior work showed that INM retention of Sun2 requires aa residues 1–158 of the NP domain, which contains the lamin binding region, NLS and ER retrieval signal but is missing the majority of the AH (Turgay et al., 2010). Sun2-Sun1 chimeras that contained the Sun2 NP domain including the AH (Sun2(1-209)-Sun1(220-716) or (Sun2[1-180]-Sun1[191-716]) were dispersed in the ER in CTDNEP1 KO cells similar to full length Sun2-mNG (Fig. S4 C). This result is consistent with a role for the NP domain and AH in retaining Sun2 at the INM and suggests that the luminal domain of Sun1 is not able to override this sensitivity to loss of CTDNEP1. Deletion of the Sun2 AH in a Sun2-Sun1 chimera that contained aa residues 1-150 of the Sun2 NP domain (Sun2[1-150]-Sun1[156-716]) retained enrichment at the NE of CTDNEP1 KO cells (Fig. S4 C). This result is consistent with the AH of Sun2 serving as a key element that confers sensitivity of INM retention of Sun2 to loss of CTDNEP1. It is also

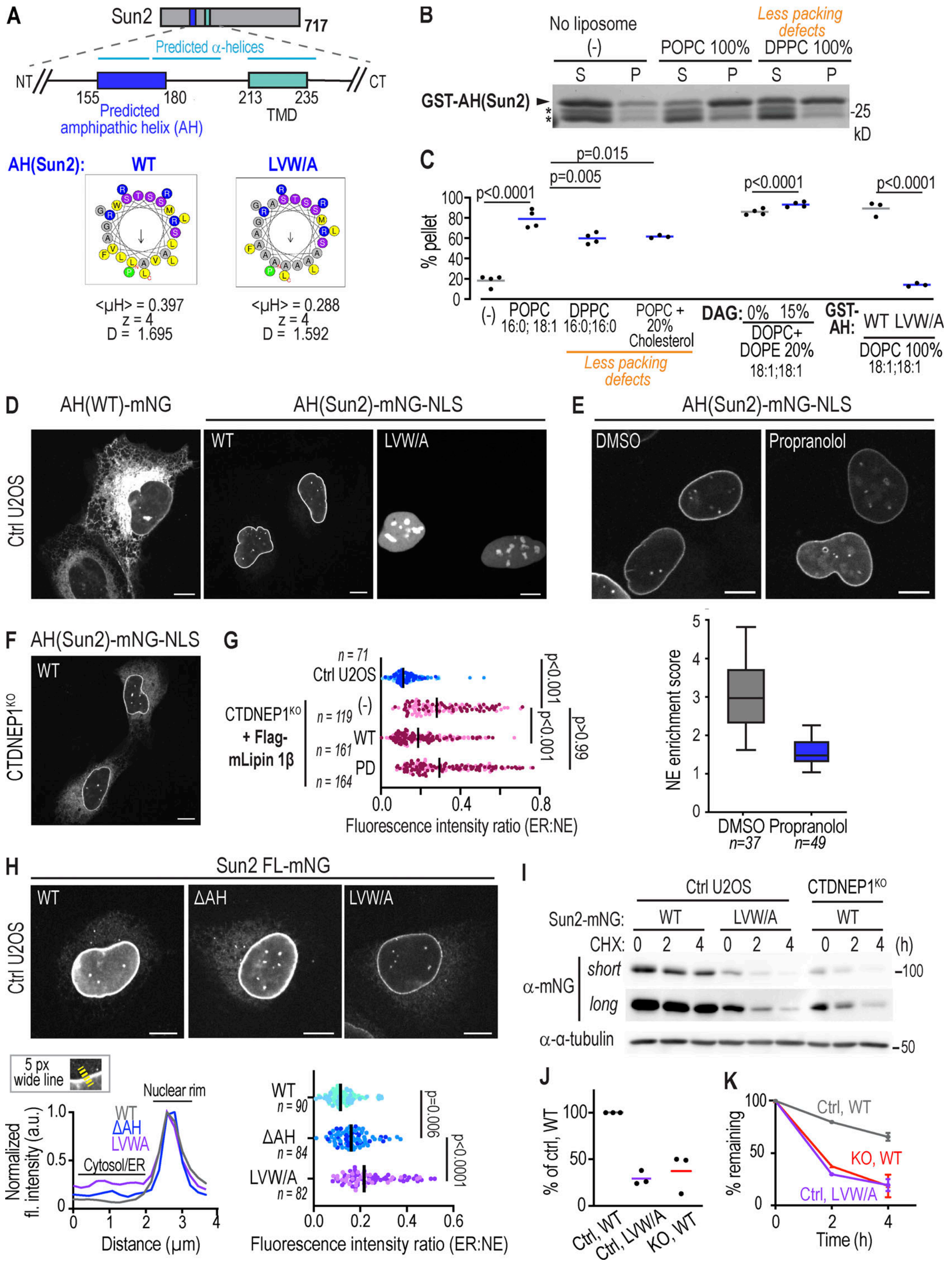

Figure 3. **Sun2 contains a membrane binding amphipathic helix that is sensitive to the INM lipid environment. (A)** Schematic of N-terminal region of Sun2 highlighting predicted amphipathic helix (AH; residues 155–180) and mutation of bulky hydrophobic residues. Helical wheel projections generated by HeliQuest with hydrophobic moment <μH>, net charge z, and the discriminant factor D. **(B and C)** Representative image of coomassie stained gel of indicated in vitro purified proteins after liposome-cosedimentation assays with indicated lipid compositions. Arrowhead: GST-AH; Asterisk: purification byproduct. In C, percent of protein in pellet as a ratio of soluble fraction is shown. *n* = 3 or 4 experimental replicates. P values: ordinary one-way ANOVA followed by Tukey's multiple comparisons test. **(D)** Spinning disk confocal images of live U2OS cells expressing indicated constructs. **(E)** Spinning disk confocal images of live U2OS cells expressing AH-mNG-NLS treated as indicated. Box plot: NE enrichment scores pooled from two independent experiments. *n* indicates the number of cells quantified. **(F)** Spinning disk confocal image of live CTDNEP1 KO cells expressing AH-mNG-NLS. **(G)** Plot of ER:NE fluorescence ratio of AH-mNG-NLS in indicated cells pooled from two or three independent experiments. *n* indicates the number of cells quantified. Bars indicate median. **(H)** Spinning disk confocal images of live U2OS cells expressing indicated constructs. Plot (left): Fluorescence intensity of mNG normalized to maximum fluorescence along line scan. Plot (right): ER:NE fluorescence ratio. P values, Kruskal–Wallis test followed by Dunn's multiple comparisons test. *n* indicates the number of cells quantified. Bars indicate median. **(I–K)** Immunoblot of whole cell lysates from cells treated with cycloheximide for indicated hours expressing indicated constructs. In J, plot shows mNG level at 0 h (untreated cells). Each dot indicates an independent experiment. In K, plot shows *n* = 2 (2 h) or 3 (4 h) independent experiments. Mean (and SD where *n* = 3) shown. All scale bars: 10 µm. Source data are available for this figure: SourceData F3.

possible that sequences in proximity of the Sun2 AH (aa 180–209), which also encode for predicted hydrophobic helices, contribute to its mislocalization to the ER in CTDNEP1 KO cells.

The Sun1 and Sun2 lamin-binding regions reside at the very N-terminus of the NP domain (1-138 in Sun1 and 1-129 in Sun2; Haque et al., 2010). A chimera in which the NP domain of Sun2 including its AH is swapped with that of Sun1 (Sun1[1-219]-Sun2 [213-717]) enriched at the NE in CTDNEP1 KO cells to the same extent as full length Sun1-mNG (Fig. S4 D). Swapping the lamin-binding region of Sun2 with that of Sun1 (Sun1[1-138]-Sun2[126-717]) was sufficient for the Sun1-Sun2 chimera to enrich at the NE in CTDNEP1 KO cells even with an intact Sun2 AH (Fig. S4 D). This suggests that aa 1–138 of Sun1 that include its lamin-binding region retains Sun1-Sun2 chimeras at the NE and overrides the sensitivity of the AH of Sun2 to the INM lipid environment. It is also possible that elements in the Sun2 NP region function coordinately with the Sun2 AH to cause its sensitivity to loss of CTDNEP1. These data highlight the different mechanisms that enrich Sun1 and Sun2 at the NE.

The chimera data suggest that the AH of Sun2 acts in concert with elements in the NP domain that also contribute to INM retention of Sun2 in control cells. Mutation of the bulky hydrophobic residues in the Sun2 AH to disrupt its membrane association (LVW/A) caused greater mislocalization of full length Sun2-mNG to the ER than an internal deletion of the Sun2 AH (Fig. 3 H). Thus, a reduced membrane binding capacity of the Sun2 AH disrupts INM retention of Sun2 to a greater extent than complete loss of the AH. These data support the idea that the membrane-dissociated form of the AH may cooperate with an additional element in the NP region to regulate Sun2 retention/levels at the INM.

The membrane-binding amphipathic helix in Sun2 is linked to its regulation degradation by the proteasome

We reasoned that membrane binding of the Sun2 AH could be linked to preventing its proteasomal degradation to stably retain Sun2 at the INM. Sun2-mNG protein with a mutated AH that no longer binds to the INM (AH-LVW/A) is at lower steady state levels and is short-lived compared to wild-type Sun2-mNG in control U2OS cells (Fig. 3, I–K). The degradation kinetics of the Sun2-mNG mutated in its AH so that it cannot bind to membranes (AH-LVW/A mutant) is similar to that of wild-type Sun2-mNG in CTDNEP1 KO cells (Fig. 3, I–K). Deletion of the AH of Sun2 only slightly decreases its steady-state expression level (Fig. S5 A) and retention at the INM (Fig. 3 H) suggesting that the AH segment contributes to its regulated degradation when not bound to membranes. A mutant version of Sun2-mNG in which two key serine residues in a motif that resembles a non-canonical SCF$^{b\text{-}trcp}$ degron (Frescas and Pagano, 2008; Krshnan et al., 2022a) were mutated to alanine (2xSA) is long-lived (Fig. 4, A and B; and Fig. S5 B). A study done in parallel to ours (Krshnan et al., 2022b *Preprint*; Lee et al., 2022 *Preprint*) provided further characterization of the SCF$^{b\text{-}trcp}$-dependent degradation mechanism of Sun2, including direct binding and recognition of these serine residues by SCF$^{b\text{-}trcp}$ (Krshnan et al., 2022a). We found that mutating the serine residues restored INM retention of Sun2-mNG mutated in its AH (2xSA and AH-LVW/A mutant) in control U2OS cells (Fig. S5 C; see also Fig. 3 H). Similarly, in CTDNEP1 KO cells the 2xSA mutation restored INM retention of full length Sun2 with its AH intact (Fig. S5 C; see also Fig. S4 B).

Together, these data suggest that dissociation of the Sun2-AH from the INM contributes to its proteasomal degradation through a neighboring sequence ("Ser-cluster"). We suggest that the "Ser-cluster" acts coordinately with the AH segment of Sun2, thus providing a mechanism to enable Sun2 degradation in a disrupted INM lipid environment. A feature of the AH when not adsorbed to membranes contributes to the reduced INM retention of Sun2 and makes the protein short-lived.

The nuclear envelope associated pool of Sun2 is targeted for proteasomal degradation

To test if the INM pool of Sun2 is targeted for proteasomal degradation, which would fit with our model that direct INM-binding by the AH of Sun2 contributes to its stabilization, we monitored the levels of the existing pool of endogenous Sun2 or Sun2-mNG in cells treated with cycloheximide following acute depletion of CTDNEP1 using the auxin (indole-3-acetic acid, IAA)-inducible degron (AID) system in DLD-1 cells (Natsume et al., 2016; Nishimura et al., 2009; Fig. 4 C). Treatment with IAA induced rapid degradation (within 1–2 h and up to 24 h) of CTDNEP1 tagged at the endogenous locus with the mAID degron and HA (Fig. S5 D) and a concomitant decrease of endogenous Sun2 protein levels over time (IAA alone in Fig. 4 D), which is consistent with the reduction in Sun2 protein levels we observed in CTDNEP1 KO cells and in cells RNAi-depleted for CTDNEP1 (Fig. S2 B and Fig. 2 B). Acute depletion of CTDNEP1 combined with cycloheximide to inhibit translation of new protein revealed the rapid kinetics of degradation of the existing Sun2 protein pool upon loss of CTDNEP1 (CHX + DMSO or IAA in Fig. 4 D). Live imaging of Sun2-mNG upon acute depletion of CTDNEP1 showed an acceleration in the loss of Sun2-mNG fluorescence signal at the nuclear rim as compared to control DMSO treated cells (Fig. 4 E). RNAi-depletion of SCF$^{b\text{-}trcp}$ stabilized the NE-associated pool of Sun2-mNG in cells acutely depleted of CTDNEP1 (Fig. 4 F; and Fig. S5, E and F). The ER-associated pool of Sun2-mNG had similar trends in the rate of loss of fluorescence intensity when CTDNEP1 was acutely inhibited (Fig. S5 G). The loss of Sun2-mNG fluorescence signal from the NE and its dependence on SCF$^{b\text{-}trcp}$ indicates that the INM-associated pool of Sun2 is a target for proteasomal degradation. The fact that the ER-associated pool of Sun2-mNG is also unstable upon loss of CTDNEP1 suggests that Sun2 loss occurs throughout the ER and NE when lipid composition is not tightly regulated, possibly because of weakened membrane association via its AH.

Discussion

Our data suggest a model in which a membrane-binding amphipathic helix (AH) is part of the mechanism that promotes the INM accumulation of the nucleo-cytoskeletal linker Sun2 (Fig. 4 G). Membrane dissociation of the AH is linked to Sun2 destabilization, which is regulated by proteasomal degradation

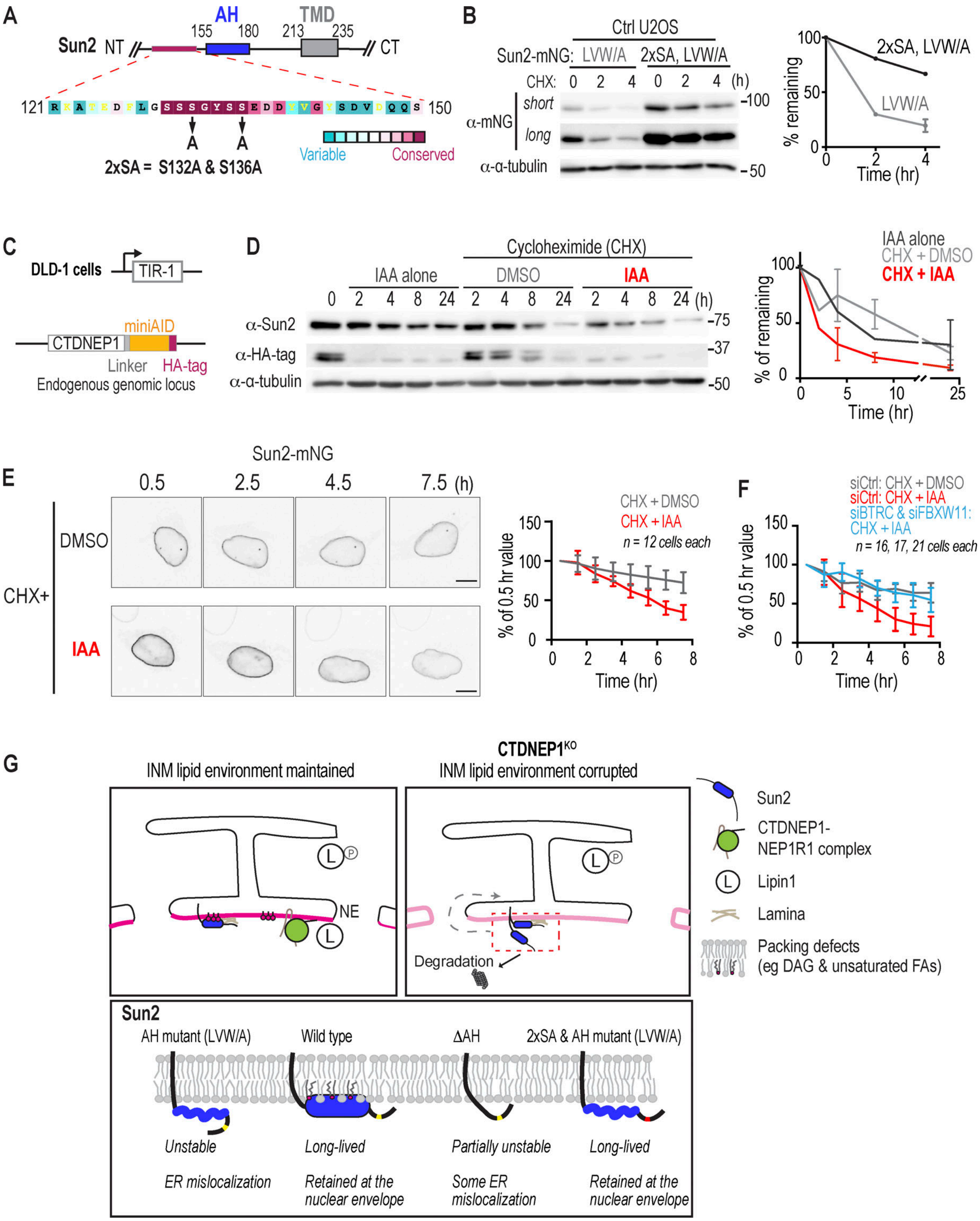

Figure 4. **Proteasomal degradation of Sun2 occurs locally at the NE and involves its membrane-binding amphipathic helix.** **(A)** Schematic of human Sun2 with amino acid residues 121–150 highlighted with colors representing ConSurf conservation scores of vertebrate Sun2 protein sequences. **(B)** Immunoblot of whole cell lysates from cells expressing indicated constructs. Plot shows *n* = 2 or 3 (LVW/A, 4 h) independent experiments. Mean (and SD where *n* = 3) shown. **(C)** Schematic of CTDNEP1^mAID-HA. **(D)** Immunoblot of whole cell lysates from DLD-1 OsTIR-1 CTDNEP1(EN)-mAID-HA cells treated as indicated. Plot shows normalized Sun2 levels of *n* = 2 (IAA alone and all 2 h) or three independent experiments. Mean (and SD where *n* = 3) shown. **(E and F)** Time-lapse confocal images of transiently expressing Sun2-mNG in live DLD-1 CTDNEP1^mAID-HA cells stably expressing OsTIR-1, treated as indicated. Plots show mNG fluorescence intensity at nuclear rim as % of the value at 0.5 h. *n* indicates the number of cells quantified pooled from two independent experiments. Scale bar, 10 µm. **(G)** Schematic model representation showing that the AH of Sun2 linked to local proteasomal degradation contributes to the retention of Sun2 at unique subdomains of the INM maintained by CTDNEP1 control of lipin 1(left). Bottom: Alterations in the membrane properties of the INM leads to weak association of the Sun2 AH to membrane lipids and exposes upstream “Ser-cluster” necessary to target Sun2 to proteasomal degradation. Source data are available for this figure: SourceData F4.

via a neighboring "Ser-cluster" (Fig. 4 G, bottom). AHs are known to be unfolded in solution but adopt a helical conformation when bound to membranes (Drin and Antonny, 2010). Weaker membrane association of the AH could favor a conformation that exposes the "Ser-cluster" to accelerate Sun2's turnover rate (Fig. 4 G). This mechanism could provide a way to regulate Sun2 in response to changes in lipid packing resulting from mechanical forces imposed on the NE (e.g., release from stretching) or metabolic changes in bilayer lipids (e.g., signaling).

Prior work has shown that the NP domain (lamin binding, NLS and ER retrieval signal) of Sun2 is necessary for its INM retention (Turgay et al., 2010). This is in line with our data that the AH alone is not the sole factor that retains full length Sun2 at the INM. Our data show that disruption of the membrane-binding capacity of the Sun2 AH impacts Sun2 retention by functioning coordinately with other retention mechanisms that include regulation by the proteasome (Fig. 4 G, lower panel).

We show that the INM environment sensed by Sun2 is regulated by CTDNEP1/lipin 1. Our INM-DAG biosensor based on the C1ab domain of PKCtheta provides a read-out of the unique lipid environment of the INM in animal cells. Lipidomics analysis of CTDNEP1 KO cells revealed that the percentage of two major DAG species containing PUFAs (e.g., arachidonic acid, 20:4) are decreased. Lipin 1 does not have a preference for acyl chain saturation or length (Han and Carman, 2010). Thus it is possible that under normal conditions, lipin 1 activity maintains a broad repertoire of DAG species including PUFA-containing DAG, which cannot be fully compensated by the upregulation of cytosolic Mg^{2+}-independent PAP activity resulting from loss of CTDNEP1 (Merta et al., 2021). A global decrease in the percentage of PUFA-cotaining lipids may also result from the increased flux in mono-unsaturated fatty acid synthesis in CTDNEP1 KO cells to balance the level of membrane unsaturation (Merta et al., 2021).

Whether PUFA-containing DAG species are specific to the INM is unknown. The C1b domain of PKCtheta that we used to develop the INM-DAG biosensor has a preference for PUFA-containing DAG species (Carrasco and Merida, 2004). Purified nuclei have been shown to be enriched in PUFA-containing phospholipids (Surette and Chilton, 1998; Williams et al., 2000). Furthermore, the PUFA arachidonic acid is released as a signaling molecule when cytosolic phospholipase A2 is localized to the INM upon NE stretch (Enyedi et al., 2016; Lomakin et al., 2020; Venturini et al., 2020). The lack of curvature at the INM instrinsically limits packing defects and so a relative enrichment of cone shaped lipids that contain PUFAs and/or small headgroups such as DAG at the INM may allow for regulation of local proteins by direct membrane sensing.

Although our data places DAG as a key determinant of INM lipid identity, we propose that the bulk properties of the INM lipid environment is specialized beyond a single lipid species. In addition to the concentration of specific DAG species at the INM, the INM-DAG biosensor is likely detecting overall changes in bulk properties of the membrane such as electrostatic charge and packing defects, as has been shown for the C1b domain of PKCtheta (Melowic et al., 2007). In most cases, AHs sense bulk membrane properties rather than specific lipid species (Drin and Antonny, 2010; Giménez-Andrés et al., 2018; Horchani et al., 2014). Thus, we prefer a model in which, the INM, despite its continuity with the ER, maintains unique bulk membrane properties that contribute to the association of membrane-binding regions such as the INM-DAG biosensor and the Sun2 AH. Interestingly, the AH of CCTα only associates with the INM under conditions of lipid stress (high PE/PC ratio; Haider et al., 2018). The AHs in nucleoporins associate with the curved nuclear pore membrane (Mészáros et al., 2015; Vollmer et al., 2015) that are not co-localized with Sun2 (Liu et al., 2007). Future work that tests the membrane properties preferred by the AH of Sun2 and that enrich for CTDNEP1/lipin 1 activity will help determine the distinct nature of INM lipid environment within specific domains.

Our work reveals a potential contribution of the membrane binding AH to the physiological functions of Sun2, including maintenance of nuclear morphology (Donahue et al., 2016; Krshnan et al., 2022a) and nuclear positioning via actin (Luxton et al., 2010; Zhu et al., 2017). Nuclear morphology defects result from overexpression of a degradation-resistant version of Sun2 (Krshnan et al., 2022a) and CTDNEP1 is necessary for nuclear positioning via the actin cytoskeleton suggesting both processes may involve lipid metabolism related effects on Sun2 (Calero-Cuenca et al., 2021). Interestingly, Nem1, the CTDNEP1 homologue in budding yeast, genetically interacts with Mps3, a yeast SUN-domain protein, and mutations in *mps3* result in altered lipid metabolism (Friederichs et al., 2012; Friederichs et al., 2011). Thus, crosstalk between nucleo-cytoskeletal linkage and INM lipids may be evolutionarily conserved, although the precise mechanisms may differ.

Our data, combined with the work of others, show that the INM harbors a unique lipid composition across multiple organisms. A common theme is a role for CTDNEP1 in NE-dependent processes including NE sealing, NPC biogenesis, nuclear size regulation, NE breakdown, and nuclear positioning (Bahmanyar et al., 2014; Calero-Cuenca et al., 2021; Jacquemyn et al., 2021; Mall et al., 2012; Mauro et al., 2022 *Preprint*; Penfield et al., 2020). These processes may require maintenance of the INM lipid environment by CTDNEP1, although much remains to be discovered about the different roles of CTDNEP1 that may be independent of lipin 1 (Rallabandi et al., 2023). Furthermore, how general functions in ER lipid homeostasis influence these processes, including Sun2 at the INM, requires further investigation. Proteomics studies have identified over 100 proteins that associate with the NE (Cheng et al., 2019; Korfali et al., 2010; Korfali et al., 2012; Schirmer et al., 2003; Wilkie et al., 2011). Our in silico analysis predicts the presence of AHs in several resident INM proteins (Fig. S5 H). Although the mode of regulation may differ, determining the repertoire of INM proteins that respond to local lipid metabolism through direct membrane binding as exemplified by Sun2 is an important future direction. Furthermore, future work that determines mechanisms that control the distribution of specific lipid species at the INM, especially given its continuity with the rest of the ER, may reveal how this specialized domain of the ER is established and defined.

Materials and methods

Plasmid construction

General note

Insertion of gene sequence was conducted either by using restriction enzymes from New England Biolabs, Gibson Assembly (E5510S; New England Biolabs) or In-Fusion HD Cloning Plus (638909; Takara). Site-directed mutagenesis was performed either by whole-plasmid PCR followed by circularization or by QuikChange Multi Site-Directed Mutagenesis Kit (200515; Agilent). Successful cloning was confirmed by sequencing for all constructs. A bipartite NLS from *Xenopus laevis* nucleoplasmin (KRPAATKKAGQAKKKK; Dingwall et al., 1988; Robbins et al., 1991; Sołtysik et al., 2019) was used.

INM-DAG biosensor

mNG-NLS was first made by inserting mNG ([Shaner et al., 2013]; cDNA was a gift from Hiroyuki Arai [University of Tokyo, Tokyo, Japan]) followed by NLS in place of EGFP in pEGFP-C2. mNG-NLS-1xC1ab was generated by inserting the coding sequence of C1ab domains (a gift from Isabel Mérida [CNB, Madrid, Spain]), which corresponds to residues 157–284 of human protein kinase C theta (NP_001310194.1; [Carrasco and Merida, 2004]). mNG-NLS-2xC1ab (INM-DAG biosensor) was generated by inserting another C1ab domain sequence after the first one leaving SRPVLC linker residues in between. The tryptophan mutant was generated by mutating the tryptophans in both C1b domains to glycines, which correspond to W253 in full-length human protein kinase C theta.

Sun2-/Sun1-mNG and their chimeras and mutants

The coding sequence for human full-length Sun2 (a gift from M. King and P. Lusk [Yale University, New Haven, CT, USA]; [Chalfant et al., 2019; May and Carroll, 2018]; NP_001186509.1) followed by mNG sequence was subcloned under a clipped CMV promoter (CMVΔ5; [Morita et al., 2012]) by replacing GFP-CHMP7 coding sequence in CMVΔ5-GFP-CHMP7 vector. Sun1 cDNA (716 aa) was isolated by PCR from total cDNA of control U2OS cell line, which was prepared by reverse transcription from total RNA using the iScript Reverse Transcription Supermix (1708840; Bio-Rad). The isolated Sun1 isoform was found to lack the exons 4 and 5 in comparison with the canonical isoform (NM_001130965.3; UniProt ID O94901-8) and was not found in RefSeq proteins of human Sun1 in NCBI Gene database (last search on May 31, 2022), thus appeared to be a novel isoform. The cDNA was inserted between CMVΔ5 and mNG to make Sun1-mNG. Sun2-Sun1 chimeras were generated by fusing the indicated portions from Sun2 and Sun1 under CMVΔ5 promoter by using In-Fusion HD Cloning Plus (Takara). AH-mNG was first generated by replacing the full-length Sun2 in Sun2-mNG vector with AH sequence (Sun2 aa 151–180), and then NLS was inserted after mNG to generate AH-mNG-NLS. Sun2 LVW/A mutant was generated by alanine substitution of L155, V159, L165, L166, W167 and V169 of Sun2. Sun2 2xSA mutant was generated by alanine substitution of S132 and S136.

Flag-hLipin 1

Flag-hLipin 1β^{RR} (wild-type or D714E) was subcloned from hLipin 1β^{RR}-EGFP constructs (gift from Toyoshi Fujimoto [Juntendo University, Tokyo, Japan]; [Sołtysik et al., 2021]).

Mammalian cell lines

U2OS, DLD-1, and HEK293 cells were grown at 37°C in 5% CO2 in DMEM low glucose (11885; Gibco) supplemented with 10% heat inactivated FBS (F4135) and 1% antibiotic-antimycotic (15240112; Gibco). U2OS mNG-NLS-2xC1ab stable cells were grown in the media supplemented with 1 µg/ml puromycin. Cells were used for experiments before reaching passage 25. Cells were tested for mycoplasma upon initial thaw and generation of new cell lines (13100-01; Southern Biotech), and untreated cells were continuously profiled for contamination by assessment of extranuclear DAPI staining.

Plasmid and siRNA transfection

For both plasmid and siRNA transfection, cells were seeded to reach 50–80% density on the day of transfection. DNA transfections were performed with Lipofectamine 2000 (11668; Thermo Fisher Scientific) in Opti-MEM (31985; Gibco) with DNA concentrations ranging from 50 to 300 ng DNA per cm^2 of growth surface. Cells were imaged or processed after 48 h (for Flag-Lipin 1 [mouse and human], Flag-DGAT1, Venus-DGAT2) or 24 h (others).

RNAi was performed using Dharmafect 1 (T-2001; Horizon Discovery) or Lipofectamine RNAiMAX (13778100; Thermo Fisher Scientific) in Opti-MEM according to the manufacturer's protocol with final siRNA concentration at 20 nM. Cell media was changed on the next day of transfection. When confluent, cells were replated 48 h after transfection. Cells were processed 72 h after transfection.

For co-transfection of siRNA and plasmids, siRNA transfection was first performed, and media was changed 6 h after transfection. On the next day, plasmid transfection was performed. Cells were processed 48 h after plasmid transfection.

CRISPR-Cas9 genome editing for generating knockin cell lines

U2OS CTDNEP1^EGFP cell line

Guide RNA sequences were designed using the online CRISPR tool http://crispr.mit.edu and reported no off-target matches: 5′-TGGGATGCCGTCTGATGCCC-3′. The guide RNA sequences were synthesized as two oligos with BbsI overhangs and an additional guanidine base 5′ to the protospacer sequence, and the oligos were cloned into pSPCas9(BB)-2A-Puro (PX459) v2.0 into BbsI site. This vector is hereafter called pX459 CTDNEP1_HR. Homology repair template (CTDNEP1-6xGly-EGFP HR) that harbors 6xGly linker sequence before EGFP and 800 bp-homology arms was generated from pEGFP-N1.

U2OS cells were transfected with pX459 CTDNEP1_HR and CTDNEP1-6xGly-EGFP HR vectors with Lipofectamine 2000, then treated with 3 µg/ml puromycin for 48 h. The remaining cells were grown up and then fluorescent cells were sorted using BD FACSAria. Sorted cells were plated sparsely into a 10-cm culture dish. Cell colonies were trypsinized and picked up with sterile filter paper disks and further grown up in 24-well plates. DNA was extracted from each clone using QiaAmp mini kit, and genotyping PCR and sequencing were performed to select clones that lacked wild-type alleles and had the integration of EGFP into CTDNEP1 loci.

DLD-1 OsTIR-1 CTDNEP1^{EN}-mAID-HA cell line

The same guide RNA sequence was used as the one used for the endogenous CTDNEP1^EGFP U2OS cell line. Vector transfection and colony selection was performed according to Yesbolatova et al. (2019) with modifications. Briefly, the guide RNA-PX459 vector and CTDNEP1-mAID-HA HR template were transfected into DLD-1 OsTIR-1 stable cells (gift from A. Holland [Johns Hopkins University]) using FuGENE HD (Promega E2311). One day after transfection, cells were collected by trypsinization. Then, collected cells were diluted in media containing final 700 µg/ml G418 and plated in a 10 cm dish. Colonies were trypsinized and picked with filter paper disks, transferred to 96-well plates. Cells were further grown up and duplicated to two 24-well plates and grown until reaching sub-confluency, then either frozen using Bambanker DIRECT medium (Nippon Genetics CS-06-001), or collected with DirectPCR working solution (0.5× DirectPCR Lysis Reagent-Cell [Viagen Biotech, 302-C] containing 0.5 mg/ml of Proteinase K). DirectPCR solution was incubated at 55°C for 6 h then at 85°C for 1.5 h to inactivate Proteinase K. PCR was performed with CloneAmp for genotyping or sequencing (Table1).

Generation of mNG-NLS-2xC1ab (INM-DAG biosensor) stable cell lines

U2OS mNG-NLS-2xC1ab stable cell lines were generated by retroviral transduction. Retroviruses were generated by transfecting HEK293T cells with pCG-gag-pol, pCMV-VSVG and pMXs-IP-mNeonGreen-NLS-2xC1ab using Lipofectamine 2000. The retroviruses were used to transduce U2OS cells and cells were selected under 1.0 µg/ml puromycin for 2 wk. Then, cells with fluorescent levels around median range were sorted by BD FACSAria and plated sparsely to a 10-cm culture dish. Cell colonies were trypsinized and picked up with paper filter disks, and further grown up in 24-well plates. For clones that showed no obvious growth anomaly or morphological alteration compared to control U2OS cells, expression level as well as absence of degraded form of the biosensor were checked by immunoblot against mNG, and the biosensor localization at nuclear rim was tested by live imaging.

Drug treatment

Drug/compound treatment was done as follows: propranolol: 100 µM for 5 min; TOFA: 10 µM for 24 h; Cycloheximide: 25 µg/ml; MLN4924: 1 µM for 24 h; IAA: 500 µM. Vehicle control was prepared by diluting the same amount of DMSO as the drug treatment counterpart.

Immunofluorescene

Cells on coverslips were fixed in 4% paraformaldehyde (+0.1% glutaraldehyde for analyzing an ER marker such as GFP-Sec61β) in PBS for 15 min at room temperature, permeabilized in 0.1% Triton X-100 for 3 min at room temperature, then blocked in 3% BSA in PBS for 30 min at room temperature. For digitonin permeabilization, cells were permeabilized with 10 µg/ml digitonin on ice for 10 min. Samples were then incubated with primary antibodies in 3% BSA in PBS for 1.5 h at room temperature or for overnight at 4°C. Samples were washed with PBS three times, then incubated with secondary antibodies in 3% BSA in PBS for 45 min at room temperature in the dark with rocking. Samples were then washed with PBS three times. Coverslips were mounted with ProLong Gold Antifade reagent with DAPI. Primary antibody concentration: anti-Sun2 (generated by C. Carroll lab, used only in Fig. 2 A) 1:1,000; anti-Sun2 (generated by C. Schlieker lab, used in other experiments) 1:1,000; anti-LBR 1:250; anti-SUN1 1:250; anti-Lamin A/C 1:1,000; anti-Lamin B1 1:1,000; anti-mNeonGreen 1:1,000; mouse anti-HA 1:1,000; anti-Flag 1:1,000.

Live-cell imaging

For live imaging, cells were plated in µ-Slide 8 Well Glass Bottom chamber (80827; ibidi). Samples were imaged in a CO_2-, temperature-, and humidity-controlled Tokai Hit Stage Top Incubator. The imaging media used was Fluorobrite DMEM (A1896701; Gibco) supplemented with 10% FBS, 2 mM L-glutamine (A2916801; Gibco) and 1% antibiotic-antimycotic (15240112; Gibco).

For live imaging of Sun2-mNG with cycloheximide, cell media was exchanged for the media containing 25 µg/ml cycloheximide and 500 µM IAA as indicated, then imaging was initiated after 30 min of the media change.

Microscopy

Fixed cell imaging and live cell imaging without time lapse were performed on an inverted Nikon Ti microscope equipped with a Yokogawa CSU-X1 confocal scanner unit with solid state 100-mW 488-nm and 50-mW 561-nm lasers, using a 60× 1.4 NA plan Apo oil immersion objective lens, and a Hamamatsu ORCA R-2 Digital CCD Camera. Live cell time-lapse imaging was performed on an inverted Nikon Ti Eclipse microscope equipped with a Yokogawa CSU-W1 confocal scanner unit with solid state 100 mW 405, 488, 514, 594, 561, 594, and 640 nm lasers, using a 60× 1.4 NA plan Apo oil immersion objective lens and/or 20× plan Fluor 0.75 NA multi-immersion objective lens, and a prime BSI sCMOS camera.

Image analysis

NE enrichment score of INM-DAG sensor

Raw image data were semi-automatically measured with a custom ImageJ Macro code (see Fig. S1 C for a schematic) and measurement results were analyzed with a custom Python code. First, the user was prompted by the macro to count the number of cell nuclei that were amenable to quantification. Cell nuclei with wrinkles or any abnormal shape were not included in quantification because these structural changes tended to blur the boundary between nuclear membrane and nucleoplasm and thus hampered correct measurement. Then, a nucleus on an optimal z frame was manually selected by a rectangle. Following the selection, the macro continued on the following process. The nucleus image was cropped (called "Whole nucleus") and auto-segmented by Li method, and the ROI for the whole nucleus was defined. In some cases, in particular when the overall intensity was low, the auto-segmentation failed to find the nucleus, and no ROI was defined. Results from those cases were excluded later on, and the Python code was based on area

Table 1. **Key reagents and resource**

Reagent or Resource	Source	Identifier
Antibodies		
Rabbit anti-Sun2	Christian Schlieker lab (Yale University) (Rose et al., 2014)	N/A
Rabbit anti-Sun2	Christopher Carroll lab (Yale University)	N/A
Rabbit anti-LBR	Christopher Carroll lab (Yale University)	N/A
Rabbit anti-Sun1	Atlas antibodies	Cat# HPA008346, RRID:AB_1080462
Mouse anti-Lamin A/C	Santa Cruz Biotechnology	Cat# sc-376248, RRID:AB_10991536
Rabbit anti-Lamin B1	Abcam	Cat# ab16048, RRID:AB_443298
Rabbit anti-emerin	Proteintech	Cat# 10351-1-AP, RRID:AB_2100056
Rabbit anti-Lipin 1	Millipore Sigma	Cat# ABS400 (discontinued)
Rabbit anti-NRF2	Abcam	Cat# ab62352, RRID:AB_944418
Mouse anti-mNeonGreen	ChromoTek	Cat# 32f6-100, RRID:AB_2827566
Mouse anti-HA	Enzo	Cat# ENZ-ABS120
Rabbit anti-HA	Cell Signaling Technologies	Cat# 3724; RRID: AB_1549585
Rabbit anti-Flag	Sigma-Aldrich	Cat# F3165, RRID:AB_259529
Mouse anti-tubulin alpha	Millipore	Cat# 05-829, RRID:AB_310035
Bacterial and virus strains		
E. coli BL21(DE3) cells	New England Biolabs	Cat# C2527
Chemicals, peptides, and recombinant proteins		
Propranolol	Millipore Sigma	Cat# 537075
Puromycin	Thermo Fisher	Cat# A1113803
TOFA	Cayman Chemicals	Cat# 10005263
1-palmitoyl-2-oleoyl-sn-glycero-3-phosphocholine (POPC) (chloroform)	Avanti	Cat# 850457C
18:1 (Δ9-Cis) PC (DOPC)	Avanti	Cat# 850375C
18:1 (Δ9-Cis) PE (DOPE)	Avanti	Cat# 850725C
18:1 DG (DAG)	Avanti	Cat# 800811C
1,2-dipalmitoyl-sn-glycero-3-phosphocholine (DPPC)	Avanti	Cat# 850355C
Cholesterol	Sigma-Aldrich	Cat# C3045
Pierce Glutathione Agarose	Thermo Fisher Scientific	Cat# 16100
Digitonin	Sigma-Aldrich	Cat# D5628
Cycloheximide	Cell Signaling	Cat# 2112
3-Indoleacetic acid (IAA)	Sigma-Aldrich	Cat# I3750
ProLong Gold Antifade Mountant with DAPI	Thermo Fisher Scientific	Cat# P36935
Experimental models: Cell lines		
U2OS	Slack lab (Harvard Medical School)	N/A
U2OS CTDNEP1^EGFP	This study	N/A
U2OS mNeonGreen-NLS-2xC1ab (INM-DAG biosensor) stable	This study	N/A
DLD-1 OsTIR-1 stable	(Holland et al., 2012)	N/A
DLD-1 OsTIR-1 stable CTDNEP1^{EN}-mAID-HA	This study	N/A
HEK293T	Breslow lab (Yale University)	N/A
Oligonucleotides		
siGENOME non-targeting siRNA Pool #2	Dharmacon	Cat# D-001206-14-05

Table 1. **Key reagents and resource (*Continued*)**

Reagent or Resource	Source	Identifier
CTDNEP1 SMARTpool siRNA	(Merta et al., 2021) Dharmacon	Cat# M-017869-00-0005
Lipin 1 custom single siRNA, no modifications: 5′-GAAUGGAAU GCCAGCUGAA-3′	(Brohée et al., 2015; Sołtysik et al., 2021) Dharmacon	N/A
Silencer select siRNA against human LMNA	Thermo Fisher	Cat# AM16708; assay ID 144426
BTRC&FBXW11 custom single siRNA (targeting both genes), no modifications: 5′-GUGGAAUUUGUGGAACAUC-3′	(Kim et al., 2015) Dharmacon	N/A
qPCR primer: Hs Sun2 forward: 5′-TGACGTGCCTGACGTATGG-3′	Primer Bank (Wang et al., 2012)	PrimerBank ID 313760642c1
qPCR primer: Hs Sun2 reverse: 3′-AAATGTGGCGATGAGTCT CTG-5′	Primer Bank	PrimerBank ID 313760642c1
qPCR primer: Hs CTDNEP1 forward: 5′-CATTTACCTTCTGCGGAG GC-3′	(Merta et al., 2021)	N/A
qPCR primer: Hs CTDNEP1 reverse: 3′-CACCTGGGCTAGCCGATT C-5′	(Merta et al., 2021)	N/A
qPCR primer: Hs 36B4 forward: 5′-AACATGCTCAACATCTCCCC-3′	(Neuhaus et al., 2011)	N/A
qPCR primer: Hs 36B4 reverse: 3′-CCGACTCCTCCGACTCTTC-5′	(Neuhaus et al., 2011)	N/A
Recombinant DNA		
CTDNEP1-GFP HR template	This study	N/A
pSPCas9(BB)-2A-Puro (PX459) v2.0	(Ran et al., 2013)	Cat #62988; RRID: Addgene_62988
pX459 CTDNEP1_HR7	This study	N/A
POM121-mCherry	(Dultz et al., 2008)	Euroscarf #P30554
sfCherry2(1-10)	(Feng et al., 2017)	RRID:Addgene_82602
sfCherry2(11)_H2B	(Feng et al., 2017)	RRID:Addgene_82605
pcDNA CTDNEP1-sfCherry2(1-10)	This study	N/A
Flag-sfCherry2(1-10)-NEP1R1	This study	N/A
sfCherry2(11)-EGFP-H2B	This study	N/A
mNeonGreen-NLS	This study	N/A
mNeonGreen-NLS-1xC1ab	This study	N/A
mNeonGreen-NLS-2xC1ab (INM-DAG biosensor)	This study	N/A
mNeonGreen-NLS-2xC1ab (2xWG)	This study	N/A
pCMV-VSV-G	(Matsudaira et al., 2017)	N/A
pCG-Gal-Pol	(Matsudaira et al., 2017)	N/A
pMXs-IP-EGFP	(Matsudaira et al., 2017)	N/A
pMXs-IP-mNeonGreen-NLS-2xC1ab	This study	N/A
CTDNEP1-mAID-HA wild-type	This study	N/A
CTDNEP1-mAID-HA D67E	This study	N/A
pRK5 Flag-mLipin 1β (mouse) wild-type	(Peterson et al., 2011)	RRID: Addgene_32005
pRK5 Flag-mLipin 1β (mouse) D712/D714E	This study	N/A
Flag-hLipin 1β^{RR} (human, resistant to siLipin 1) wild-type	This study	N/A
Flag-hLipin 1β^{RR} (human, resistant to siLipin 1) D714E	This study	N/A
Flag-DGAT1 (mouse) wild-type	(Sołtysik et al., 2021; Xu et al., 2012)	N/A
Flag-DGAT1 (mouse) H426A	This study	N/A
mScaret-I-DGAT1 (mouse) wild-type	This study	N/A
mScaret-I-DGAT1 (mouse) H426A	This study	N/A
Venus-DGAT2 (human) wild-type	(Sołtysik et al., 2021; Xu et al., 2012)	N/A

Table 1. **Key reagents and resource (*Continued*)**

Reagent or Resource	Source	Identifier
Venus-DGAT2 (human) H163A	This study	N/A
GFP-Sec61β	Gia Voeltz lab	N/A
GFP-CHMP7 under CMVΔ5	(Gu et al., 2017)	RRID: Addgene_97006
Sun2 (human)-mNeonGreen	This study	N/A
Sun1 (human)-mNeonGreen	This study	N/A
Sun1(1-219)-Sun2(213-717)-mNeonGreen	This study	N/A
Sun2(1-209)-Sun1(220-716)-mNeonGreen	This study	N/A
Sun1(1-138)-Sun2(126-717)-mNeonGreen	This study	N/A
Sun2(1-180)-Sun1(191-716)-mNeonGreen	This study	N/A
Sun2(1-150)-Sun1(156-716)-mNeonGreen	This study	N/A
pGEX-6P-1 GST-AH	This study	N/A
pGEX-6P-1 GST-AH (LVW/A)	This study	N/A
AH-mNeonGreen	This study	N/A
AH-mNeonGreen-NLS	This study	N/A
AH(LVW/A)-mNeonGreen-NLS	This study	N/A
Sun1(156-190) (Sun1-AH)-mNeonGreen-NLS	This study	N/A
HA-AH-mNeonGreen-NLS	This study	N/A
Sun2 (LVW/A)-mNeonGreen	This study	N/A
Sun2 (2xSA)-mNeonGreen	This study	N/A
Sun2 (2xSA- LVW/A)-mNeonGreen	This study	N/A
pMK292 (mAID-mCherry2-NeoR)	(Natsume et al., 2016)	RRID:Addgene_72830
CTDNEP1-mAID-HA HR template	This study	N/A
Software and algorithms		
FIJI	(Schindelin et al., 2012)	https://imagej.net/Fiji
GraphPad Prism 9	GraphPad Software	https://www.graphpad.com/scientificsoftware/prism/
SnapGene	GSL Biotech LLC	https://www.snapgene.com/
ImageJ file name encrypter	Astha Jaiswal, Holger Lorenz	https://imagej.net/plugins/blind-analysis-tools
ImageJ StarDist	(Schmidt et al., 2018)	https://imagej.net/plugins/stardist
TMHMM	(Krogh et al., 2001)	https://services.healthtech.dtu.dk/service.php?TMHMM-2.0
PEP-FOLD3	(Lamiable et al., 2016; Thévenet et al., 2012)	https://bioserv.rpbs.univ-paris-diderot.fr/services/PEP-FOLD3/
HeliQuest	(Gautier et al., 2008)	https://heliquest.ipmc.cnrs.fr/
MemBrain	(Feng et al., 2022)	http://www.csbio.sjtu.edu.cn/bioinf/MemBrain/
AmphipaSeeK	(Combet et al., 2000; Sapay et al., 2006)	https://npsa-prabi.ibcp.fr/cgi-bin/npsa_automat.pl?page=/NPSA/npsa_amphipaseek.html
Clustal Omega	(Madeira et al., 2022; Sievers et al., 2011)	https://www.ebi.ac.uk/Tools/msa/clustalo/
ConSurf	(Ashkenazy et al., 2016; Ashkenazy et al., 2010)	https://consurf.tau.ac.il/
Python version 3.8	Python Software Foundation	https://www.python.org/
Anaconda	Anaconda Inc	https://www.anaconda.com/products/distribution

value = 0. To measure intensity from "intra-nucleus" (i.e., nucleus area excluding nuclear rim), a mask image was generated by performing "Erosion" three times of the binary image that was generated from the ROI. This mask was multiplied with "Whole nucleus" image by "Image Calculator" to leave signals only from the intra-nucleus area (called "Intra-nucleus"). Total intensity within the ROI was measured for "Whole-nucleus" and "Intra-nucleus." Total intensity of the binary mask within the ROI was also measured, which gives a value that is equal to the value of the area of "Intra-nucleus." The total intensity and area values of the "Nuclear rim" were obtained by subtraction of the values of "Intra-nucleus" from "Original nucleus." Mean value of "Whole nucleus" and "Nuclear rim" were calculated by dividing the total intensity by the area of each. Finally, after subtraction of background mean value, the ratio of "Nuclear rim" to "Intra-nucleus" was calculated to give the "NE enrichment score." The measurement was repeated for all cells in images in a given directory. The measurement results were exported to CSV files and analyzed by Python Pandas, Matplotlib, and Seaborn libraries. Statistical analysis was performed by Tukey HSD test using the Python Statsmodels library.

Sun2/Sun1 NE localization

Endogenous Sun2/Sun1 NE localization was categorized into three bins: "strong," "moderate," and "non" based on visual impression of the clarity and brightness of Sun2/Sun1 localization at the nuclear rim. Categorization was performed blindly by using File Name Encrypter in Blind Analysis Tools of Fiji on file names.

Sun2 expression intensity in nucleus area

Raw image data were automatically measured with a custom ImageJ Macro code and measurement results were analyzed with a custom Python code. Firstly, images were max-projected and split to DAPI, Flag-tag (absent in case for siCDS/PIS experiments), and Sun2 channels. Then, from DAPI channel, ROIs for nuclear area were defined by StarDist plugin with the default settings. Within the ROIs, mean intensity values of DAPI, tag, and Sun2 as well as area were measured and exported to a CSV file. The resulting CSV files were concatenated and analyzed using Python Pandas, NumPy, Matplotlib, and Seaborn libraries. Background was subtracted from Sun2 intensity. In most cases background = 2,000 was applied. Flag tag-positive cells were determined based on a threshold value, which was determined by examination of several raw images. Typically mean Flag intensity = 3,000 was applied. Mitotic cells and small DAPI signals including cell debris and micronuclei were excluded from analysis based on relatively high intensity of DAPI and small area size, respectively. After subtraction of background value, Sun2 intensity was normalized against the mean value of cells without tag expression in each transfection condition. Statistical analysis was performed by Tukey HSD test using the Python Statsmodels library.

NE enrichment of Sun2/Sun1 and its chimera/mutants (ER/NE ratio)

In a given image on Fiji, a line with 5-pixel width and 5-µm length was drawn from cytoplasm to nucleus, centered on the nuclear rim. The maximum value along the line was considered the "NE" value. The average value of the first 5 pixels along the line (namely 5 × 5 pixels) was considered the "ER/cytoplasm" value. Average value from the cell-free area was used to subtract background. Then the ER/NE ratio was calculated.

Nucleus enrichment of mNG-NLS (cytosol/nucleoplasm ratio)

Mean intensity values of manually drawn rectangular regions (5 × 5 pixels) were measured in cytosolic and nucleoplasmic area. When necessary, brightness/contrast was modified to visually distinguish cytosolic area from non-cell area. Nucleoli were avoided when drawing a nucleoplasm region for measurement. Average value from the cell-free area was used to subtract background. Then the cytosol:nucleoplasm ratio was calculated.

Sun2-mNG intensity at NE and ER under IAA treatment

Similarly to NE enrichment analysis, line scan was performed with a line crossing the nuclear rim. The maximum intensity was considered Sun2-mNG intensity at the NE, and the average value of the first 5 pixels along the line (namely 5 × 5 pixels) was considered the ER value.

Immunoprecipitation

Cell where pelleted by trypsinization and centrifugation at 300 × *g* for 5 min followed by 1× PBS wash, after pelleting the cells, they were lysed by adding lysis buffer (0.1% Triton X-100, 50 mM NaF, 1 mM EDTA, 1 mM EGTA, 10 mM Na_2HPO_4, 50 mM *b*-glycerophosphate, 1 tablet/50 ml cOmplete protease inhibitor cocktail [11836153001; Roche] pH 7.4). Lysates were homogenized by pushing through a 23G needle 30 times and then centrifuged at >20,000 × *g* for 10 min at 4°C. Preconjugated anti-HA magnetic beads (88836; Thermo Fisher Scientific) were washed twice with TBST and equilibrated in lysis buffer without detergent. 10% of the total volume of lysed cells was transferred to a new tube labelled input, the remaining 90% volume was added to equilibrated anti-HA beads and incubated for 2 h rocking at 4°C. Anti-HA beads were then washed twice with TBST and 4× loading dye was added to denature the beads and load samples to SDS-PAGE gel.

Immunoblot

Cells were lysed with ice-cold RIPA buffer (25 mM Tris pH 7.4, 1% NP-40, 0.5% sodium deoxycholate, 0.1% SDS, 150 mM NaCl, and 1 tablet/50 ml cOmplete Mini protease inhibitor cocktail [11836153001; Roche]) with cell scraper, incubated on ice for 15 min, and then centrifuged at >20,000 × *g* (15,000 rpm) for 15 min at 4°C. Protein concentration was determined using the Pierce BCA Protein assay kit (23225; Thermo Fisher Scientific). 10-15 µg of whole cell lysates/lane were run on 8–15% polyacrylamide gels dependent on target size, and protein was wet transferred to 0.22 µm nitrocellulose membranes (1620112; Bio-Rad). Membranes were blocked in 5% nonfat dry milk in TBS (for lipin 1) or 1 or 3% BSA in PBS (for targets other than lipin 1) for 30 min. Membranes were then incubated with primary antibodies in milk or BSA for 1.5 h at room temperature or overnight at 4°C with rocking. Membranes were washed three times for 5 min in TBST, then incubated with goat anti-mouse or rabbit IgG secondary antibodies (31430 or 31460; Thermo Fisher Scientific) in 5% milk in TBST for 45 min at room temperature with rocking. Membranes were washed three times for 5 min in TBST. Clarity or Clarity Max ECL reagent (1705060S, 1705062S; Bio-Rad) was used to visualize chemiluminescence, and images were taken with a Bio-Rad ChemiDoc Imaging System. Bands on immunoblot were quantified using Fiji. Antibody concentration was the following: anti-Sun1, Lipin 1, HA, NRF2, 1:1,000; anti-Lamin A/C, Sun2 (Carroll lab), mNeonGreen 1:3,000; α-tubulin 1:5,000; secondary antibodies 1:10,000.

Cycloheximide chase assay

Cell media was exchanged with 25 µg/ml cycloheximide. After the indicated time, cells were collected for immunoblot. mNG or HA-tag bands on immunoblot were quantified and normalized to that of α-tubulin, and is shown as % of the value of 0 h.

Lipidomics

Cell collection and lipid extraction for mass spectrometry lipidomics

Early-passage cells were counted by hemocytometer, suspended in PBS at a concentration of 3×10^6 cells/ml, and flash frozen in liquid nitrogen. Triplicate samples were submitted for each condition, and corresponding triplicate samples were lysed and protein extracted and protein concentration determined by Pierce BCA assay. Mass spectrometry-based lipid analysis was performed by Lipotype GmbH as described (Sampaio et al., 2011). Lipids were extracted using a two-step chloroform/methanol procedure (Ejsing et al., 2009). Samples were spiked with internal lipid standard mixture containing: cardiolipin 14:0/14:0/14:0/14:0 (CL), ceramide 18:1;2/17:0 (Cer), diacylglycerol 17:0/17:0 (DAG), hexosylceramide 18:1;2/12:0 (HexCer), lyso-phosphatidate 17:0 (LPA), lyso-phosphatidylcholine 12:0 (LPC), lyso-phosphatidylethanolamine 17:1 (LPE), lyso-phosphatidylglycerol 17:1 (LPG), lyso-phosphatidylinositol 17:1 (LPI), lyso-phosphatidylserine 17:1 (LPS), phosphatidate 17:0/17:0 (PA), phosphatidylcholine 17:0/17:0 (PC), phosphatidylethanolamine 17:0/17:0 (PE), phosphatidylglycerol 17:0/17:0 (PG), phosphatidylinositol 16:0/16:0 (PI), phosphatidylserine 17:0/17:0 (PS), cholesterol ester 20:0 (CE), sphingomyelin 18:1;2/12:0;0 (SM), triacylglycerol 17:0/17:0/17:0 (TAG). After extraction, the organic phase was transferred to an infusion plate and dried in a speed vacuum concentrator. In the first step, the dry extract was re-suspended in 7.5 mM ammonium acetate in chloroform/methanol/propanol (1:2:4, V:V:V), and in the second step, dry extract in 33% ethanol solution of methylamine in chloroform/methanol (0.003:5:1; V:V:V). All liquid handling steps were performed using Hamilton Robotics STARlet robotic platform with the Anti Droplet Control feature for organic solvents pipetting.

MS data acquisition

Samples were analyzed by direct infusion on a QExactive mass spectrometer (Thermo Fisher Scientific) equipped with a TriVersa NanoMate ion source (Advion Biosciences). Samples were analyzed in both positive and negative ion modes with a resolution of $R_{m/z=200} = 280{,}000$ for MS and $R_{m/z=200} = 17{,}500$ for MSMS experiments, in a single acquisition. MSMS was triggered by an inclusion list encompassing corresponding MS mass ranges scanned in 1 Da increments (Surma et al., 2015). Both MS and MSMS data were combined to monitor CE, DAG, and TAG ions as ammonium adducts; PC, PC O-, as acetate adducts; and CL, PA, PE, PE O-, PG, PI, and PS as deprotonated anions. MS only was used to monitor LPA, LPE, LPE O-, LPI, and LPS as deprotonated anions; Cer, HexCer, SM, LPC, and LPC O- as acetate adducts.

Data analysis and post-processing

Data were analyzed with in-house developed lipid identification software based on LipidXplorer (Herzog et al., 2012; Herzog et al., 2011). Data post-processing and normalization were performed using an in-house developed data management system. Only lipid identifications with a signal-to-noise ratio >5, and a signal intensity fivefold higher than in corresponding blank samples were considered for further data analysis.

Quantitative real-time PCR

RNA was harvested using the RNeasy Mini kit (74104; Qiagen) using the manufacturer's protocol, using Qiashredders (79654; Qiagen) for tissue homogenization and with additional RNase-free DNase (79254; Qiagen) treatment after the first RW1 wash and subsequently adding another RW1 wash. RNA was eluted with RNAse-free water and diluted to 50 ng/µl. RNA was subject to reverse transcription using the iScript Reverse Transcription Supermix (1708840; Bio-Rad) with 400 ng RNA per reaction. The subsequent cDNA was diluted 1:5 for RT-qPCR. cDNA was analyzed for RT-PCR using the iTaq universal SYBR Green Supermix (1725120; Bio-Rad) with the CFX384 Touch Real-Time PCR Detection System (Bio-Rad). Production of a single amplicon was confirmed by melt curve analysis. Cycle threshold values were analyzed using the ΔΔCt method.

Recombinant protein purification

GST-tagged proteins were expressed in *E. coli* BL21(DE3) cells. Cells were grown at 37°C to an OD600 nm of 0.6–0.9 and then cooled at 20°C. Protein expression was induced with isopropyl βD-1-thiogalactopyranoside (IPTG) at 20°C for 16 h, and cells were harvested by centrifugation and stored at −80°C. Frozen cells were resuspended in buffer A (1× PBS, 1 mM EDTA, 1 mM EGTA, pH 8.0) and lysed by sonication. After adding DTT and CHAPS detergent at final 1 mM and 2% w/v concentration, respectively, sample was centrifuged at 20,000 rpm with Beckman Coulter type 70 Ti rotor at 4°C for 30 min. The supernatant was incubated with pre-equilibrated Pierce Glutathione Agarose at 4°C for 1 h. The resin was centrifuged at 2,000 rpm at 4°C for 2 min, washed three times with buffer B (50 mM Tris-HCl pH 8.0, 150 mM NaCl, 1 mM DTT, 1% CHAPS) and transferred to pre-wet Econo-Pac Chromatography Columns (7321010; Bio-Rad). Protein was eluted with buffer C (50 mM Tris-HCl pH 8.0, 150 mM NaCl, 10 mM reduced glutathione, 0.7% CHAPS), aliquoted and analyzed by SDS-PAGE and Coomassie blue stain. Fractions containing the protein were diluted threefold in buffer C so that the final CHAPS concentration is below its critical micelle concentration, which is 0.4–0.6%. The diluted fractions were dialyzed in 1× PBS using Slide-A-Lyser Dialysis Cassette G2

10,000 MWCO 15 ml (87731; Thermo Fisher Scientific). Dialyzed protein solution was concentrated roughly threefold by centrifugation with Amicon Ultra-15 Centrifugal Filter Unit (UFC901024; Millipore) at 4,000 rpm at 4°C for 15 min, then flash-frozen and stored at −80°C until used.

Liposome co-sedimentation

Lipid mixtures were dried under nitrogen gas and then under vacuum for 1 h at room temperature. Dried lipids were hydrated liposome-binding buffer (20 mM HEPES-NaOH pH 7.4, 150 mM NaCl, 1 mM $MgCl_2$, 1 mM DTT) for 60 min at 37°C, vortexed for 1 min, and subjected to three rounds of freeze-thaw cycles with liquid nitrogen. To remove protein aggregates, the protein solution was subjected to centrifugation using a TLA120 fixed angle rotor (Beckman) at 55,000 rpm for 15 min at 4°C before use. 10 µg of proteins were incubated with 50 nmol liposomes for 10 min at room temperature, and the mixture was centrifuged at 55,000 rpm for 30 min at 20°C using a TLA120 fixed angle rotor (Beckman). The resultant supernatant and pellet were subjected to SDS–PAGE, and the proteins and lipids were stained with Coomassie blue. The intensities of individual bands were quantified with Fiji.

Secondary structure analysis

Secondary structure analysis was done with PEP-FOLD3. HeliQuest was used to generate a helical wheel projection and to obtain hydrophobic moment <µH> and net charge Z values, which yielded a discriminant factor D = 0.944 (<µH>) + 0.33 (z) that predicts the possibly of the AH being a lipid-binding helix, as described in HeliQuest (https://heliquest.ipmc.cnrs.fr/HelpProcedure.htm). MemBrain 3.1 and AmphipaSeek web servers were used to predict AHs in the protein sequence of Sun2 (Q9UH99-1), Sun1 (O94901-8), LEMD2 (Q8NC56-1), Man1 (Q9Y2U8), Nemp1 (O14524-1), Nemp2 (A6NFY4-1), LBR (Q14739), and emerin (P50402).

Conservation score analysis

Amino-acid sequences of putative Sun2 orthologues in jawed vertebrates were obtained from the list of “Orthologs” of human Sun2 in NCBI Gene database. Species were chosen such that they include birds, turtles, alligators, lizards, mammals, amphibians and cartilaginous fishes. The sequence of the zebrafish homologue, which was not found in the list, was obtained from HomoloGene in NCBI database (ID: 9313). Accession numbers of proteins are the following: *Homo sapiens*: NP_001186509.1; *Pan troglodytes* (chimpanzee): XP_016794668.1; *Canis lupus familiaris* (dog): XP_538371.3; *Bos taurus* (cow): NP_001095789.1; *Mus musculus*: NP_001192274.1; *Rattus norvegicus*: XP_235483.6; *Phyllostomus hastatus* (bat): XP_045690878.1; *Gallus gallus* (chicken): XP_040525101.1; *Pogona vitticeps* (bearded dragon): XP_020643298.1; *Chelonia mydas* (sea turtle): XP_037737727.1; *Xenopus tropicalis* (frog): XP_012817972.2; *Rhinatrema bivittatum* (caecilian): XP_029446057.1; *Danio rerio* (zebrafish): XP_001919691.1; *Amblyraja radiata* (skate): XP_032869439.1. A multiple sequence alignment and phylogenetic tree were generated using Clustal Omega with the default settings. The conservation score was obtained using the ConSurf server with the default settings by providing the multiple sequence alignment (query: human Sun2) and phylogenetic tree as inputs. Low confidence in the score was presented as yellow color of a residue.

Statistical analysis

GraphPad Prism 8 was used for all statistical analysis otherwise specified in methods. Color-coding of each experiment repetition was based on Superplot (Lord et al., 2020). Sample size required for reliable statistical analysis was determined before performing experiments using Sample Size Calculator (https://clincalc.com/stats/samplesize.aspx). Statistical tests used, sample sizes, definitions of *n* and *N*, and P values are reported in figures and/or figure legends.

Online supplemental material

Fig. S1 is related to Fig. 1 and shows that CTDNEP1/NEP1R1 can reach the INM, a plot of the lipidomics analysis of percentage of DAG species in CTDNEP1 KO cells, and the image analysis pipeline for “NE enrichment score.” Fig. S2 is related to Fig. 2 and provides further support for selective loss of Sun2 protein at the nuclear rim in CTDNEP1 KO cells and that it is dependent on SCF^{bTRCP} and DAG metabolism. Fig. S3 is related to Fig. 3 and shows further characterization of the AH of Sun2 in vitro and in vivo as a membrane associated protein segment that targets the INM when fused to an NLS in control U2OS cells, but targets both the ER and INM in CTDNEP1 KO cells, unlike a predicted AH in Sun1. Fig. S4 is related to Fig. 3 and shows the protein levels and localizations of chimeric Sun2/Sun1 constructs. Fig. S5 is related to Fig. 4 and shows that mutation in the AH and serine rich regions of Sun2 affect its protein stability, the dependence of Sun2 protein stability on SCF^{bTRCP} and the presence of predicted AH sequences in other NE-associated proteins.

Data availability

Raw data generated in this study are available upon request to the Lead Contact. ImageJ Macro and Python codes are found at GitHub (https://github.com/shokenlee/Lee_2022_Sun2-Lipid).

Acknowledgments

We thank M. Hochstrasser, J.M. Gendron, C. Schlieker (Yale University, New Haven, CT, USA) and G. Drin (CNRS, Valbonne, France) for helpful discussions; I. Mérida (CNB, Madrid, Spain), H.Y. Mak (Hong Kong University of Science and Technology, Hong Kong, China), T. Fujimoto (Juntendo University, Tokyo, Japan), T. Niki (RIKEN, Saitama, Japan), H. Arai (University of Tokyo, Tokyo, Japan), A. Frost (UCSF, San Francisco, CA, USA), J. Ellenberg (EMBL, Heidelberg, Germany), A. Maryniak and A. Holland (Johns Hopkins University, Baltimore, MD, USA), C. Schlieker (Yale University), and Topher Carroll (former Yale School of Medicine) for reagents. We thank E. Rodriguez, M. King and C.P. Lusk (Yale School of Medicine) for distributing reagents; S. Chou (Yale University) for technical support on protein purification; J. Yang and Y. Zhang (Yale School of Medicine) and J. Nikolaus (Yale University) for technical support on liposome experiments; C. Chan and J.W. Emerson (Yale University) for support on statistical analysis; K. Nelson (Yale University) for the support on flow cytometry; Yale Nucleus Club and BB Club for helpful discussions.

This work was supported by: National Institutes of Health (NIH) grant R01 (GM131004) to S. Bahmanyar. Additional support is by Anderson Postdoctoral Fellowship to S. Lee, NIH (T32s GM100884 and GM007499) and the Gruber Foundation to H. Merta, and NIH (T32 GM722345) to J.W. Carrasquillo Rodríguez.

Author contributions: S. Lee and S. Bahmanyar conceived the project. S. Lee performed most of the experiments and data analysis. J.W. Carrasquillo Rodríguez performed experiments for CTDNEP1/NEP1R1 localization and immunoprecipitation and provided data that guided the DAG biosensor experiments. H. Merta generated the CTDNEP1^EGFP cell line. S. Lee wrote the IJ Macro and Python scripts. S. Lee and S. Bahmanyar wrote the manuscript with input from other authors. S. Bahmanyar supervised the project.

Disclosures: The authors declare no competing interests exist.

Submitted: 6 April 2023
Revised: 22 May 2023
Accepted: 2 June 2023

References

Adam, S.A., R.S. Marr, and L. Gerace. 1990. Nuclear protein import in permeabilized mammalian cells requires soluble cytoplasmic factors. *J. Cell Biol.* 111:807–816. https://doi.org/10.1083/jcb.111.3.807

Ashkenazy, H., S. Abadi, E. Martz, O. Chay, I. Mayrose, T. Pupko, and N. Ben-Tal. 2016. ConSurf 2016: An improved methodology to estimate and visualize evolutionary conservation in macromolecules. *Nucleic Acids Res.* 44:W344–W350. https://doi.org/10.1093/nar/gkw408

Ashkenazy, H., E. Erez, E. Martz, T. Pupko, and N. Ben-Tal. 2010. ConSurf 2010: Calculating evolutionary conservation in sequence and structure of proteins and nucleic acids. *Nucleic Acids Res.* 38:W529–W533. https://doi.org/10.1093/nar/gkq399

Bahmanyar, S., R. Biggs, A.L. Schuh, A. Desai, T. Müller-Reichert, A. Audhya, J.E. Dixon, and K. Oegema. 2014. Spatial control of phospholipid flux restricts endoplasmic reticulum sheet formation to allow nuclear envelope breakdown. *Genes Dev.* 28:121–126. https://doi.org/10.1101/gad.230599.113

Bahmanyar, S., and C. Schlieker. 2020. Lipid and protein dynamics that shape nuclear envelope identity. *Mol. Biol. Cell.* 31:1315–1323. https://doi.org/10.1091/mbc.E18-10-0636

Barbosa, A.D., K. Lim, M. Mari, J.R. Edgar, L. Gal, P. Sterk, B.J. Jenkins, A. Koulman, D.B. Savage, M. Schuldiner, et al. 2019. Compartmentalized synthesis of triacylglycerol at the inner nuclear membrane regulates nuclear organization. *Dev. Cell.* 50:755–766.e6. https://doi.org/10.1016/j.devcel.2019.07.009

Baron, C.L., and V. Malhotra. 2002. Role of diacylglycerol in PKD recruitment to the TGN and protein transport to the plasma membrane. *Science.* 295:325–328. https://doi.org/10.1126/science.1066759

Baumann, O., and B. Walz. 2001. Endoplasmic reticulum of animal cells and its organization into structural and functional domains. *Int. Rev. Cytol.* 205:149–214. https://doi.org/10.1016/s0074-7696(01)05004-5

Behnia, R., and S. Munro. 2005. Organelle identity and the signposts for membrane traffic. *Nature.* 438:597–604. https://doi.org/10.1038/nature04397

Belaadi, N., L. Pernet, J. Aureille, G. Chadeuf, M. Rio, N. Vaillant, E. Vitiello, L. Lafanechère, G. Loirand, and C. Guilluy. 2022. SUN2 regulates mitotic duration in response to extracellular matrix rigidity. *Proc. Natl. Acad. Sci. USA.* 119:e2116167119. https://doi.org/10.1073/pnas.2116167119

Boni, A., A.Z. Politi, P. Strnad, W. Xiang, M.J. Hossain, and J. Ellenberg. 2015. Live imaging and modeling of inner nuclear membrane targeting reveals its molecular requirements in mammalian cells. *J. Cell Biol.* 209:705–720. https://doi.org/10.1083/jcb.201409133

Brohée, L., S. Demine, J. Willems, T. Arnould, A.C. Colige, and C.F. Deroanne. 2015. Lipin-1 regulates cancer cell phenotype and is a potential target to potentiate rapamycin treatment. *Oncotarget.* 6:11264–11280. https://doi.org/10.18632/oncotarget.3595

Buchwalter, A., R. Schulte, H. Tsai, J. Capitanio, and M. Hetzer. 2019. Selective clearance of the inner nuclear membrane protein emerin by vesicular transport during ER stress. *Elife.* 8:e49796. https://doi.org/10.7554/eLife.49796

Calero-Cuenca, F.J., D.S. Osorio, S. Carvalho-Marques, S.C. Sridhara, L.M. Oliveira, Y. Jiao, J. Diaz, C.S. Janota, B. Cadot, and E.R. Gomes. 2021. Ctdnep1 and Eps8L2 regulate dorsal actin cables for nuclear positioning during cell migration. *Curr. Biol.* 31:1521–1530.e1528. https://doi.org/10.1016/j.cub.2021.01.007

Carrasco, S., and I. Merida. 2004. Diacylglycerol-dependent binding recruits PKCtheta and RasGRP1 C1 domains to specific subcellular localizations in living T lymphocytes. *Mol. Biol. Cell.* 15:2932–2942. https://doi.org/10.1091/mbc.e03-11-0844

Chalfant, M., K.W. Barber, S. Borah, D. Thaller, and C.P. Lusk. 2019. Expression of TorsinA in a heterologous yeast system reveals interactions with lumenal domains of LINC and nuclear pore complex components. *Mol. Biol. Cell.* 30:530–541. https://doi.org/10.1091/mbc.E18-09-0585

Chang, W., H.J. Worman, and G.G. Gundersen. 2015. Accessorizing and anchoring the LINC complex for multifunctionality. *J. Cell Biol.* 208:11–22. https://doi.org/10.1083/jcb.201409047

Cheng, L.C., S. Baboo, C. Lindsay, L. Brusman, S. Martinez-Bartolomé, O. Tapia, X. Zhang, J.R. Yates III, and L. Gerace. 2019. Identification of new transmembrane proteins concentrated at the nuclear envelope using organellar proteomics of mesenchymal cells. *Nucleus.* 10:126–143. https://doi.org/10.1080/19491034.2019.1618175

Combet, C., C. Blanchet, C. Geourjon, and G. Deléage. 2000. NPS@: Network protein sequence analysis. *Trends Biochem. Sci.* 25:147–150. https://doi.org/10.1016/s0968-0004(99)01540-6

Cornell, R.B. 2016. Membrane lipid compositional sensing by the inducible amphipathic helix of CCT. *Biochim. Biophys. Acta.* 1861:847–861. https://doi.org/10.1016/j.bbalip.2015.12.022

Das, J., and G.M. Rahman. 2014. C1 domains: Structure and ligand-binding properties. *Chem. Rev.* 114:12108–12131. https://doi.org/10.1021/cr300481j

Dechat, T., S.A. Adam, P. Taimen, T. Shimi, and R.D. Goldman. 2010. Nuclear lamins. *Cold Spring Harb. Perspect. Biol.* 2:a000547. https://doi.org/10.1101/cshperspect.a000547

Dechat, T., K. Pfleghaar, K. Sengupta, T. Shimi, D.K. Shumaker, L. Solimando, and R.D. Goldman. 2008. Nuclear lamins: Major factors in the structural organization and function of the nucleus and chromatin. *Genes Dev.* 22:832–853. https://doi.org/10.1101/gad.1652708

Dingwall, C., J. Robbins, S.M. Dilworth, B. Roberts, and W.D. Richardson. 1988. The nucleoplasmin nuclear location sequence is larger and more complex than that of SV-40 large T antigen. *J. Cell Biol.* 107:841–849. https://doi.org/10.1083/jcb.107.3.841

Donahue, D.A., S. Amraoui, F. di Nunzio, C. Kieffer, F. Porrot, S. Opp, F. Diaz-Griffero, N. Casartelli, and O. Schwartz. 2016. SUN2 overexpression deforms nuclear shape and inhibits HIV. *J. Virol.* 90:4199–4214. https://doi.org/10.1128/JVI.03202-15

Drin, G., and B. Antonny. 2010. Amphipathic helices and membrane curvature. *FEBS Lett.* 584:1840–1847. https://doi.org/10.1016/j.febslet.2009.10.022

Dultz, E., E. Zanin, C. Wurzenberger, M. Braun, G. Rabut, L. Sironi, and J. Ellenberg. 2008. Systematic kinetic analysis of mitotic dis- and reassembly of the nuclear pore in living cells. *J. Cell Biol.* 180:857–865. https://doi.org/10.1083/jcb.200707026

Ejsing, C.S., J.L. Sampaio, V. Surendranath, E. Duchoslav, K. Ekroos, R.W. Klemm, K. Simons, and A. Shevchenko. 2009. Global analysis of the yeast lipidome by quantitative shotgun mass spectrometry. *Proc. Natl. Acad. Sci. USA.* 106:2136–2141. https://doi.org/10.1073/pnas.0811700106

Enyedi, B., M. Jelcic, and P. Niethammer. 2016. The cell nucleus serves as a mechanotransducer of tissue damage-induced inflammation. *Cell.* 165:1160–1170. https://doi.org/10.1016/j.cell.2016.04.016

Feng, S., S. Sekine, V. Pessino, H. Li, M.D. Leonetti, and B. Huang. 2017. Improved split fluorescent proteins for endogenous protein labeling. *Nat. Commun.* 8:370. https://doi.org/10.1038/s41467-017-00494-8

Feng, S.H., C.Q. Xia, P.D. Zhang, and H.B. Shen. 2022. Ab-initio membrane protein amphipathic helix structure prediction using deep neural networks. *IEEE/ACM Trans. Comput. Biol. Bioinform.* 19:795–805. https://doi.org/10.1109/TCBB.2020.3029274

Foo, S., A. Cazenave-Gassiot, M.R. Wenk, and S. Oliferenko. 2023. Diacylglycerol at the inner nuclear membrane fuels nuclear envelope expansion in closed mitosis. *J. Cell Sci.* 136:jcs260568. https://doi.org/10.1242/jcs.260568

Foresti, O., V. Rodriguez-Vaello, C. Funaya, and P. Carvalho. 2014. Quality control of inner nuclear membrane proteins by the Asi complex. *Science*. 346:751–755. https://doi.org/10.1126/science.1255638

Frescas, D., and M. Pagano. 2008. Deregulated proteolysis by the F-box proteins SKP2 and beta-TrCP: Tipping the scales of cancer. *Nat. Rev. Cancer*. 8:438–449. https://doi.org/10.1038/nrc2396

Friederichs, J.M., J.M. Gardner, C.J. Smoyer, C.R. Whetstine, M. Gogol, B.D. Slaughter, and S.L. Jaspersen. 2012. Genetic analysis of Mps3 SUN domain mutants in *Saccharomyces cerevisiae* reveals an interaction with the SUN-like protein Slp1. *G3*. 2:1703–1718. https://doi.org/10.1534/g3.112.004614

Friederichs, J.M., S. Ghosh, C.J. Smoyer, S. McCroskey, B.D. Miller, K.J. Weaver, K.M. Delventhal, J. Unruh, B.D. Slaughter, and S.L. Jaspersen. 2011. The SUN protein Mps3 is required for spindle pole body insertion into the nuclear membrane and nuclear envelope homeostasis. *PLoS Genet*. 7:e1002365. https://doi.org/10.1371/journal.pgen.1002365

Gautier, R., D. Douguet, B. Antonny, and G. Drin. 2008. HELIQUEST: A web server to screen sequences with specific alpha-helical properties. *Bioinformatics*. 24:2101–2102. https://doi.org/10.1093/bioinformatics/btn392

Giménez-Andrés, M., A. Čopič, and B. Antonny. 2018. The many faces of amphipathic helices. *Biomolecules*. 8:45. https://doi.org/10.3390/biom8030045

Gu, M., D. LaJoie, O.S. Chen, A. von Appen, M.S. Ladinsky, M.J. Redd, L. Nikolova, P.J. Bjorkman, W.I. Sundquist, K.S. Ullman, and A. Frost. 2017. LEM2 recruits CHMP7 for ESCRT-mediated nuclear envelope closure in fission yeast and human cells. *Proc. Natl. Acad. Sci. USA*. 114:E2166–E2175. https://doi.org/10.1073/pnas.1613916114

Haider, A., Y.C. Wei, K. Lim, A.D. Barbosa, C.H. Liu, U. Weber, M. Mlodzik, K. Oras, S. Collier, M.M. Hussain, et al. 2018. PCYT1A regulates phosphatidylcholine homeostasis from the inner nuclear membrane in response to membrane stored curvature elastic stress. *Dev. Cell*. 45:481–495.e8. https://doi.org/10.1016/j.devcel.2018.04.012

Hampoelz, B., A. Andres-Pons, P. Kastritis, and M. Beck. 2019. Structure and assembly of the nuclear pore complex. *Annu. Rev. Biophys*. 48:515–536. https://doi.org/10.1146/annurev-biophys-052118-115308

Han, G.S., and G.M. Carman. 2010. Characterization of the human LPIN1-encoded phosphatidate phosphatase isoforms. *J. Biol. Chem*. 285:14628–14638. https://doi.org/10.1074/jbc.M110.117747

Han, S., S. Bahmanyar, P. Zhang, N. Grishin, K. Oegema, R. Crooke, M. Graham, K. Reue, J.E. Dixon, and J.M. Goodman. 2012. Nuclear envelope phosphatase 1-regulatory subunit 1 (formerly TMEM188) is the metazoan Spo7p ortholog and functions in the lipin activation pathway. *J. Biol. Chem*. 287:3123–3137. https://doi.org/10.1074/jbc.M111.324350

Haque, F., D. Mazzeo, J.T. Patel, D.T. Smallwood, J.A. Ellis, C.M. Shanahan, and S. Shackleton. 2010. Mammalian SUN protein interaction networks at the inner nuclear membrane and their role in laminopathy disease processes. *J. Biol. Chem*. 285:3487–3498. https://doi.org/10.1074/jbc.M109.071910

Harayama, T., and T. Shimizu. 2020. Roles of polyunsaturated fatty acids, from mediators to membranes. *J. Lipid Res*. 61:1150–1160. https://doi.org/10.1194/jlr.R120000800

Herzog, R., K. Schuhmann, D. Schwudke, J.L. Sampaio, S.R. Bornstein, M. Schroeder, and A. Shevchenko. 2012. LipidXplorer: A software for consensual cross-platform lipidomics. *PLoS One*. 7:e29851. https://doi.org/10.1371/journal.pone.0029851

Herzog, R., D. Schwudke, K. Schuhmann, J.L. Sampaio, S.R. Bornstein, M. Schroeder, and A. Shevchenko. 2011. A novel informatics concept for high-throughput shotgun lipidomics based on the molecular fragmentation query language. *Genome Biol*. 12:R8. https://doi.org/10.1186/gb-2011-12-1-r8

Hetzer, M.W. 2010. The nuclear envelope. *Cold Spring Harb. Perspect. Biol*. 2:a000539. https://doi.org/10.1101/cshperspect.a000539

Hofbauer, H.F., M. Gecht, S.C. Fischer, A. Seybert, A.S. Frangakis, E.H.K. Stelzer, R. Covino, G. Hummer, and R. Ernst. 2018. The molecular recognition of phosphatidic acid by an amphipathic helix in Opi1. *J. Cell Biol*. 217:3109–3126. https://doi.org/10.1083/jcb.201802027

Holland, A.J., D. Fachinetti, J.S. Han, and D.W. Cleveland. 2012. Inducible, reversible system for the rapid and complete degradation of proteins in mammalian cells. *Proc. Natl. Acad. Sci. USA*. 109:E3350–E3357. https://doi.org/10.1073/pnas.1216880109

Horchani, H., M. de Saint-Jean, H. Barelli, and B. Antonny. 2014. Interaction of the Spo20 membrane-sensor motif with phosphatidic acid and other anionic lipids, and influence of the membrane environment. *PLoS One*. 9:e113484. https://doi.org/10.1371/journal.pone.0113484

Jacquemyn, J., J. Foroozandeh, K. Vints, J. Swerts, P. Verstreken, N.V. Gounko, S.F. Gallego, and R. Goodchild. 2021. Torsin and NEP1R1-CTDNEP1 phosphatase affect interphase nuclear pore complex insertion by lipid-dependent and lipid-independent mechanisms. *EMBO J*. 40:e106914. https://doi.org/10.15252/embj.2020106914

Ji, J., J. Shen, Y. Xu, M. Xie, Q. Qian, T. Qiu, W. Shi, D. Ren, J. Ma, W. Liu, and B. Liu. 2022. FBXO2 targets glycosylated SUN2 for ubiquitination and degradation to promote ovarian cancer development. *Cell Death Dis*. 13:442. https://doi.org/10.1038/s41419-022-04892-9

Katta, S.S., C.J. Smoyer, and S.L. Jaspersen. 2014. Destination: Inner nuclear membrane. *Trends Cell Biol*. 24:221–229. https://doi.org/10.1016/j.tcb.2013.10.006

Khmelinskii, A., E. Blaszczak, M. Pantazopoulou, B. Fischer, D.J. Omnus, G. Le Dez, A. Brossard, A. Gunnarsson, J.D. Barry, M. Meurer, et al. 2014. Protein quality control at the inner nuclear membrane. *Nature*. 516:410–413. https://doi.org/10.1038/nature14096

Kim, T.Y., P.F. Siesser, K.L. Rossman, D. Goldfarb, K. Mackinnon, F. Yan, X. Yi, M.J. MacCoss, R.T. Moon, C.J. Der, and M.B. Major. 2015. Substrate trapping proteomics reveals targets of the βTrCP2/FBXW11 ubiquitin ligase. *Mol. Cell. Biol*. 35:167–181. https://doi.org/10.1128/MCB.00857-14

Kim, Y., M.S. Gentry, T.E. Harris, S.E. Wiley, J.C. Lawrence Jr, and J.E. Dixon. 2007. A conserved phosphatase cascade that regulates nuclear membrane biogenesis. *Proc. Natl. Acad. Sci. USA*. 104:6596–6601. https://doi.org/10.1073/pnas.0702099104

Korfali, N., G.S. Wilkie, S.K. Swanson, V. Srsen, D.G. Batrakou, E.A. Fairley, P. Malik, N. Zuleger, A. Goncharevich, J. de Las Heras, et al. 2010. The leukocyte nuclear envelope proteome varies with cell activation and contains novel transmembrane proteins that affect genome architecture. *Mol. Cell. Proteomics*. 9:2571–2585. https://doi.org/10.1074/mcp.M110.002915

Korfali, N., G.S. Wilkie, S.K. Swanson, V. Srsen, J. de Las Heras, D.G. Batrakou, P. Malik, N. Zuleger, A.R. Kerr, L. Florens, and E.C. Schirmer. 2012. The nuclear envelope proteome differs notably between tissues. *Nucleus*. 3:552–564. https://doi.org/10.4161/nucl.22257

Krogh, A., B. Larsson, G. von Heijne, and E.L. Sonnhammer. 2001. Predicting transmembrane protein topology with a hidden markov model: Application to complete genomes. *J. Mol. Biol*. 305:567–580. https://doi.org/10.1006/jmbi.2000.4315

Krshnan, L., W.S. Siu, M. Van de Weijer, D. Hayward, E.N. Guerrero, U. Gruneberg, and P. Carvalho. 2022a. Regulated degradation of the inner nuclear membrane protein SUN2 maintains nuclear envelope architecture and function. *Elife*. 11:e81573. https://doi.org/10.7554/eLife.81573

Krshnan, L., W.S. Siu, M.V.d. Weijer, D. Hayward, E.N. Guerrero, U. Gruneberg, and P. Carvalho. 2022b. Regulated degradation of the inner nuclear membrane protein SUN2 maintains nuclear envelope architecture and function. *bioRxiv*. (Preprint posted July 15, 2022). https://doi.org/10.1101/2022.07.15.500172

Lamiable, A., P. Thévenet, J. Rey, M. Vavrusa, P. Derreumaux, and P. Tufféry. 2016. PEP-FOLD3: Faster de novo structure prediction for linear peptides in solution and in complex. *Nucleic Acids Res*. 44:W449–W454. https://doi.org/10.1093/nar/gkw329

Lee, S., H. Merta, J.W.C. Rodríguez, and S. Bahmanyar. 2022. A membrane sensing mechanism couples local lipid metabolism to protein degradation at the inner nuclear membrane. *bioRxiv*. (Preprint posted July 06, 2022). https://doi.org/10.1101/2022.07.06.498903

Lin, D.H., and A. Hoelz. 2019. The structure of the nuclear pore complex (an update). *Annu. Rev. Biochem*. 88:725–783. https://doi.org/10.1146/annurev-biochem-062917-011901

Liu, Q., N. Pante, T. Misteli, M. Elsagga, M. Crisp, D. Hodzic, B. Burke, and K.J. Roux. 2007. Functional association of Sun1 with nuclear pore complexes. *J. Cell Biol*. 178:785–798. https://doi.org/10.1083/jcb.200704108

Lomakin, A.J., C.J. Cattin, D. Cuvelier, Z. Alraies, M. Molina, G.P.F. Nader, N. Srivastava, P.J. Sáez, J.M. Garcia-Arcos, I.Y. Zhitnyak, et al. 2020. The nucleus acts as a ruler tailoring cell responses to spatial constraints. *Science*. 370:eaba2894. https://doi.org/10.1126/science.aba2894

Lord, S.J., K.B. Velle, R.D. Mullins, and L.K. Fritz-Laylin. 2020. SuperPlots: Communicating reproducibility and variability in cell biology. *J. Cell Biol*. 219:e202001064. https://doi.org/10.1083/jcb.202001064

Loveless, T.B., B.R. Topacio, A.A. Vashisht, S. Galaang, K.M. Ulrich, B.D. Young, J.A. Wohlschlegel, and D.P. Toczyski. 2015. DNA damage regulates translation through β-TRCP targeting of CReP. *PLoS Genet*. 11:e1005292. https://doi.org/10.1371/journal.pgen.1005292

Luxton, G.W., E.R. Gomes, E.S. Folker, E. Vintinner, and G.G. Gundersen. 2010. Linear arrays of nuclear envelope proteins harness retrograde actin flow for nuclear movement. *Science*. 329:956–959. https://doi.org/10.1126/science.1189072

Madeira, F., M. Pearce, A.R.N. Tivey, P. Basutkar, J. Lee, O. Edbali, N. Madhusoodanan, A. Kolesnikov, and R. Lopez. 2022. Search and sequence analysis tools services from EMBL-EBI in 2022. *Nucleic Acids Res.* 50:W276–W279. https://doi.org/10.1093/nar/gkac240

Majumder, S., P.T. Willey, M.S. DeNies, A.P. Liu, and G.W.G. Luxton. 2018. A synthetic biology platform for the reconstitution and mechanistic dissection of LINC complex assembly. *J. Cell Sci.* 132:jcs219451. https://doi.org/10.1242/jcs.219451

Mall, M., T. Walter, M. Gorjánácz, I.F. Davidson, T.B. Nga Ly-Hartig, J. Ellenberg, and I.W. Mattaj. 2012. Mitotic lamin disassembly is triggered by lipid-mediated signaling. *J. Cell Biol.* 198:981–990. https://doi.org/10.1083/jcb.201205103

Matsudaira, T., K. Mukai, T. Noguchi, J. Hasegawa, T. Hatta, S.I. Iemura, T. Natsume, N. Miyamura, H. Nishina, J. Nakayama, et al. 2017. Endosomal phosphatidylserine is critical for the YAP signalling pathway in proliferating cells. *Nat. Commun.* 8:1246. https://doi.org/10.1038/s41467-017-01255-3

Mauro, M.S., G. Celma, V. Zimyanin, M.M. Magaj, K.H. Gibson, S. Redemann, and S. Bahmanyar. 2022. Ndc1 drives nuclear pore complex assembly independent of membrane biogenesis to promote nuclear formation and growth. *Elife*. 11:e75513. https://doi.org/10.7554/eLife.75513

May, C.K., and C.W. Carroll. 2018. Differential incorporation of SUN-domain proteins into LINC complexes is coupled to gene expression. *PLoS One*. 13:e0197621. https://doi.org/10.1371/journal.pone.0197621

McFie, P.J., S.L. Stone, S.L. Banman, and S.J. Stone. 2010. Topological orientation of acyl-CoA:diacylglycerol acyltransferase-1 (DGAT1) and identification of a putative active site histidine and the role of the n terminus in dimer/tetramer formation. *J. Biol. Chem.* 285:37377–37387. https://doi.org/10.1074/jbc.M110.163691

Melowic, H.R., R.V. Stahelin, N.R. Blatner, W. Tian, K. Hayashi, A. Altman, and W. Cho. 2007. Mechanism of diacylglycerol-induced membrane targeting and activation of protein kinase Ctheta. *J. Biol. Chem.* 282:21467–21476. https://doi.org/10.1074/jbc.M700119200

Merta, H., J.W. Carrasquillo Rodríguez, M.I. Anjur-Dietrich, T. Vitale, M.E. Granade, T.E. Harris, D.J. Needleman, and S. Bahmanyar. 2021. Cell cycle regulation of ER membrane biogenesis protects against chromosome missegregation. *Dev. Cell.* 56:3364–3379.e10. https://doi.org/10.1016/j.devcel.2021.11.009

Mészáros, N., J. Cibulka, M.J. Mendiburo, A. Romanauska, M. Schneider, and A. Köhler. 2015. Nuclear pore basket proteins are tethered to the nuclear envelope and can regulate membrane curvature. *Dev. Cell.* 33:285–298. https://doi.org/10.1016/j.devcel.2015.02.017

Morita, E., J. Arii, D. Christensen, J. Votteler, and W.I. Sundquist. 2012. Attenuated protein expression vectors for use in siRNA rescue experiments. *Biotechniques*. 0:1–5. https://doi.org/10.2144/000113909

Natarajan, N., O. Foresti, K. Wendrich, A. Stein, and P. Carvalho. 2020. Quality control of protein complex assembly by a transmembrane recognition factor. *Mol. Cell.* 77:108–119.e9. https://doi.org/10.1016/j.molcel.2019.10.003

Natsume, T., T. Kiyomitsu, Y. Saga, and M.T. Kanemaki. 2016. Rapid protein depletion in human cells by auxin-inducible degron tagging with short homology donors. *Cell Rep.* 15:210–218. https://doi.org/10.1016/j.celrep.2016.03.001

Neuhaus, J., T. Schwalenberg, L.C. Horn, H. Alexander, and J.U. Stolzenburg. 2011. New aspects in the differential diagnosis and therapy of bladder pain syndrome/interstitial cystitis. *Adv. Urol.* 2011:639479. https://doi.org/10.1155/2011/639479

Nishimura, K., T. Fukagawa, H. Takisawa, T. Kakimoto, and M. Kanemaki. 2009. An auxin-based degron system for the rapid depletion of proteins in nonplant cells. *Nat. Methods*. 6:917–922. https://doi.org/10.1038/nmeth.1401

Penfield, L., R. Shankar, E. Szentgyörgyi, A. Laffitte, M.S. Mauro, A. Audhya, T. Müller-Reichert, and S. Bahmanyar. 2020. Regulated lipid synthesis and LEM2/CHMP7 jointly control nuclear envelope closure. *J. Cell Biol.* 219:e201908179. https://doi.org/10.1083/jcb.201908179

Peterson, T.R., S.S. Sengupta, T.E. Harris, A.E. Carmack, S.A. Kang, E. Balderas, D.A. Guertin, K.L. Madden, A.E. Carpenter, B.N. Finck, and D.M. Sabatini. 2011. mTOR complex 1 regulates lipin 1 localization to control the SREBP pathway. *Cell*. 146:408–420. https://doi.org/10.1016/j.cell.2011.06.034

Rahman, G.M., S. Shanker, N.E. Lewin, N. Kedei, C.S. Hill, B.V. Prasad, P.M. Blumberg, and J. Das. 2013. Identification of the activator-binding residues in the second cysteine-rich regulatory domain of protein kinase Cθ (PKCθ). *Biochem. J.* 451:33–44. https://doi.org/10.1042/BJ20121307

Rallabandi, H.R., H. Choi, H. Cha, Y.J. Kim. 2023. Research Trends in C-Terminal Domain Nuclear Envelope Phosphatase 1. *Life*. 13:1338. https://doi.org/https://doi.org/10.3390/life13061338

Ran, F.A., P.D. Hsu, J. Wright, V. Agarwala, D.A. Scott, and F. Zhang. 2013. Genome engineering using the CRISPR-Cas9 system. *Nat. Protoc.* 8:2281–2308. https://doi.org/10.1038/nprot.2013.143

Robbins, J., S.M. Dilworth, R.A. Laskey, and C. Dingwall. 1991. Two interdependent basic domains in nucleoplasmin nuclear targeting sequence: Identification of a class of bipartite nuclear targeting sequence. *Cell*. 64:615–623. https://doi.org/10.1016/0092-8674(91)90245-t

Romanauska, A., and A. Köhler. 2018. The inner nuclear membrane is a metabolically active territory that generates nuclear lipid droplets. *Cell*. 174:700–715.e18. https://doi.org/10.1016/j.cell.2018.05.047

Romanauska, A., and A. Köhler. 2021. Reprogrammed lipid metabolism protects inner nuclear membrane against unsaturated fat. *Dev. Cell*. 56:2562–2578.e3. https://doi.org/10.1016/j.devcel.2021.07.018

Rose, A.E., C. Zhao, E.M. Turner, A.M. Steyer, and C. Schlieker. 2014. Arresting a Torsin ATPase reshapes the endoplasmic reticulum. *J. Biol. Chem.* 289:552–564. https://doi.org/10.1074/jbc.M113.515791

Sampaio, J.L., M.J. Gerl, C. Klose, C.S. Ejsing, H. Beug, K. Simons, and A. Shevchenko. 2011. Membrane lipidome of an epithelial cell line. *Proc. Natl. Acad. Sci. USA*. 108:1903–1907. https://doi.org/10.1073/pnas.1019267108

Sapay, N., Y. Guermeur, and G. Deléage. 2006. Prediction of amphipathic in-plane membrane anchors in monotopic proteins using a SVM classifier. *BMC Bioinformatics*. 7:255. https://doi.org/10.1186/1471-2105-7-255

Schindelin, J., I. Arganda-Carreras, E. Frise, V. Kaynig, M. Longair, T. Pietzsch, S. Preibisch, C. Rueden, S. Saalfeld, B. Schmid, et al. 2012. Fiji: An open-source platform for biological-image analysis. *Nat. Methods*. 9:676–682. https://doi.org/10.1038/nmeth.2019

Schirmer, E.C., L. Florens, T. Guan, J.R. Yates III, and L. Gerace. 2003. Nuclear membrane proteins with potential disease links found by subtractive proteomics. *Science*. 301:1380–1382. https://doi.org/10.1126/science.1088176

Schmidt, U., M. Weigert, C. Broaddus, and G. Myers. 2018. Cell detection with star-convex polygons. *arXiv*. https://doi.org/10.48550/arXiv.1806.03535

Shaner, N.C., G.G. Lambert, A. Chammas, Y. Ni, P.J. Cranfill, M.A. Baird, B.R. Sell, J.R. Allen, R.N. Day, M. Israelsson, et al. 2013. A bright monomeric green fluorescent protein derived from *Branchiostoma lanceolatum*. *Nat. Methods*. 10:407–409. https://doi.org/10.1038/nmeth.2413

Shin, J.Y., and H.J. Worman. 2022. Molecular pathology of laminopathies. *Annu. Rev. Pathol.* 17:159–180. https://doi.org/10.1146/annurev-pathol-042220-034240

Sievers, F., A. Wilm, D. Dineen, T.J. Gibson, K. Karplus, W. Li, R. Lopez, H. McWilliam, M. Remmert, J. Söding, et al. 2011. Fast, scalable generation of high-quality protein multiple sequence alignments using Clustal Omega. *Mol. Syst. Biol.* 7:539. https://doi.org/10.1038/msb.2011.75

Sołtysik, K., Y. Ohsaki, T. Tatematsu, J. Cheng, and T. Fujimoto. 2019. Nuclear lipid droplets derive from a lipoprotein precursor and regulate phosphatidylcholine synthesis. *Nat. Commun.* 10:473. https://doi.org/10.1038/s41467-019-08411-x

Sołtysik, K., Y. Ohsaki, T. Tatematsu, J. Cheng, A. Maeda, S.Y. Morita, and T. Fujimoto. 2021. Nuclear lipid droplets form in the inner nuclear membrane in a seipin-independent manner. *J. Cell Biol.* 220:e202005026. https://doi.org/10.1083/jcb.202005026

Sosa, B.A., A. Rothballer, U. Kutay, and T.U. Schwartz. 2012. LINC complexes form by binding of three KASH peptides to domain interfaces of trimeric SUN proteins. *Cell*. 149:1035–1047. https://doi.org/10.1016/j.cell.2012.03.046

Spitaler, M., E. Emslie, C.D. Wood, and D. Cantrell. 2006. Diacylglycerol and protein kinase D localization during T lymphocyte activation. *Immunity*. 24:535–546. https://doi.org/10.1016/j.immuni.2006.02.013

Starr, D.A., and H.N. Fridolfsson. 2010. Interactions between nuclei and the cytoskeleton are mediated by SUN-KASH nuclear-envelope bridges. *Annu. Rev. Cell Dev. Biol.* 26:421–444. https://doi.org/10.1146/annurev-cellbio-100109-104037

Stewart, R.M., E.C. Rodriguez, and M.C. King. 2019. Ablation of SUN2-containing LINC complexes drives cardiac hypertrophy without interstitial fibrosis. *Mol. Biol. Cell*. 30:1664–1675. https://doi.org/10.1091/mbc.E18-07-0438

Stewart, R.M., A.E. Zubek, K.A. Rosowski, S.M. Schreiner, V. Horsley, and M.C. King. 2015. Nuclear-cytoskeletal linkages facilitate cross talk between the nucleus and intercellular adhesions. *J. Cell Biol.* 209: 403–418. https://doi.org/10.1083/jcb.201502024

Stone, S.J., M.C. Levin, and R.V. Farese Jr. 2006. Membrane topology and identification of key functional amino acid residues of murine acyl-CoA:diacylglycerol acyltransferase-2. *J. Biol. Chem.* 281:40273–40282. https://doi.org/10.1074/jbc.M607986200

Surette, M.E., and F.H. Chilton. 1998. The distribution and metabolism of arachidonate-containing phospholipids in cellular nuclei. *Biochem. J.* 330:915–921. https://doi.org/10.1042/bj3300915

Surma, M.A., R. Herzog, A. Vasilj, C. Klose, N. Christinat, D. Morin-Rivron, K. Simons, M. Masoodi, and J.L. Sampaio. 2015. An automated shotgun lipidomics platform for high throughput, comprehensive, and quantitative analysis of blood plasma intact lipids. *Eur. J. Lipid Sci. Technol.* 117: 1540–1549. https://doi.org/10.1002/ejlt.201500145

Thaller, D.J., D. Tong, C.J. Marklew, N.R. Ader, P.J. Mannino, S. Borah, M.C. King, B. Ciani, and C.P. Lusk. 2021. Direct binding of ESCRT protein Chm7 to phosphatidic acid-rich membranes at nuclear envelope herniations. *J. Cell Biol.* 220:e202004222. https://doi.org/10.1083/jcb.202004222

Thévenet, P., Y. Shen, J. Maupetit, F. Guyon, P. Derreumaux, and P. Tufféry. 2012. PEP-FOLD: An updated de novo structure prediction server for both linear and disulfide bonded cyclic peptides. *Nucleic Acids Res.* 40: W288–W293. https://doi.org/10.1093/nar/gks419

Tsuji, T., J. Cheng, T. Tatematsu, A. Ebata, H. Kamikawa, A. Fujita, S. Gyobu, K. Segawa, H. Arai, T. Taguchi, et al. 2019. Predominant localization of phosphatidylserine at the cytoplasmic leaflet of the ER, and its TMEM16K-dependent redistribution. *Proc. Natl. Acad. Sci. USA.* 116: 13368–13373. https://doi.org/10.1073/pnas.1822025116

Turgay, Y., R. Ungricht, A. Rothballer, A. Kiss, G. Csucs, P. Horvath, and U. Kutay. 2010. A classical NLS and the SUN domain contribute to the targeting of SUN2 to the inner nuclear membrane. *EMBO J.* 29: 2262–2275. https://doi.org/10.1038/emboj.2010.119

Ungricht, R., M. Klann, P. Horvath, and U. Kutay. 2015. Diffusion and retention are major determinants of protein targeting to the inner nuclear membrane. *J. Cell Biol.* 209:687–703. https://doi.org/10.1083/jcb.201409127

Ungricht, R., and U. Kutay. 2017. Mechanisms and functions of nuclear envelope remodelling. *Nat. Rev. Mol. Cell Biol.* 18:229–245. https://doi.org/10.1038/nrm.2016.153

Vamparys, L., R. Gautier, S. Vanni, W.F. Bennett, D.P. Tieleman, B. Antonny, C. Etchebest, and P.F. Fuchs. 2013. Conical lipids in flat bilayers induce packing defects similar to that induced by positive curvature. *Biophys. J.* 104:585–593. https://doi.org/10.1016/j.bpj.2012.11.3836

Vanni, S., H. Hirose, H. Barelli, B. Antonny, and R. Gautier. 2014. A subnanometre view of how membrane curvature and composition modulate lipid packing and protein recruitment. *Nat. Commun.* 5:4916. https://doi.org/10.1038/ncomms5916

Venturini, V., F. Pezzano, F. Català Castro, H.M. Häkkinen, S. Jiménez-Delgado, M. Colomer-Rosell, M. Marro, Q. Tolosa-Ramon, S. Paz-López, M.A. Valverde, et al. 2020. The nucleus measures shape changes for cellular proprioception to control dynamic cell behavior. *Science.* 370: eaba2644. https://doi.org/10.1126/science.aba2644

Vollmer, B., M. Lorenz, D. Moreno-Andrés, M. Bodenhöfer, P. De Magistris, S.A. Astrinidis, A. Schooley, M. Flötenmeyer, S. Leptihn, and W. Antonin. 2015. Nup153 recruits the nup107-160 complex to the inner nuclear membrane for interphasic nuclear pore complex assembly. *Dev. Cell.* 33:717–728. https://doi.org/10.1016/j.devcel.2015.04.027

Wang, X., A. Spandidos, H. Wang, and B. Seed. 2012. PrimerBank: A PCR primer database for quantitative gene expression analysis, 2012 update. *Nucleic Acids Res.* 40:D1144–D1149. https://doi.org/10.1093/nar/gkr1013

Wilkie, G.S., N. Korfali, S.K. Swanson, P. Malik, V. Srsen, D.G. Batrakou, J. de las Heras, N. Zuleger, A.R. Kerr, L. Florens, and E.C. Schirmer. 2011. Several novel nuclear envelope transmembrane proteins identified in skeletal muscle have cytoskeletal associations. *Mol. Cell Proteomics.* 10: M110.003129. https://doi.org/10.1074/mcp.M110.003129

Williams, S.D., F.F. Hsu, and D.A. Ford. 2000. Electrospray ionization mass spectrometry analyses of nuclear membrane phospholipid loss after reperfusion of ischemic myocardium. *J. Lipid Res.* 41:1585–1595. https://doi.org/10.1016/S0022-2275(20)31991-X

Xu, N., S.O. Zhang, R.A. Cole, S.A. McKinney, F. Guo, J.T. Haas, S. Bobba, R.V. Farese Jr, and H.Y. Mak. 2012. The FATP1-DGAT2 complex facilitates lipid droplet expansion at the ER-lipid droplet interface. *J. Cell Biol.* 198: 895–911. https://doi.org/10.1083/jcb.201201139

Yesbolatova, A., T. Natsume, K.I. Hayashi, and M.T. Kanemaki. 2019. Generation of conditional auxin-inducible degron (AID) cells and tight control of degron-fused proteins using the degradation inhibitor auxinole. *Methods.* 164–165:73–80. https://doi.org/10.1016/j.ymeth.2019.04.010

Zhu, R., S. Antoku, and G.G. Gundersen. 2017. Centrifugal displacement of nuclei reveals multiple LINC complex mechanisms for homeostatic nuclear positioning. *Curr. Biol.* 27:3097–3110.e5. https://doi.org/10.1016/j.cub.2017.08.073

Supplemental material

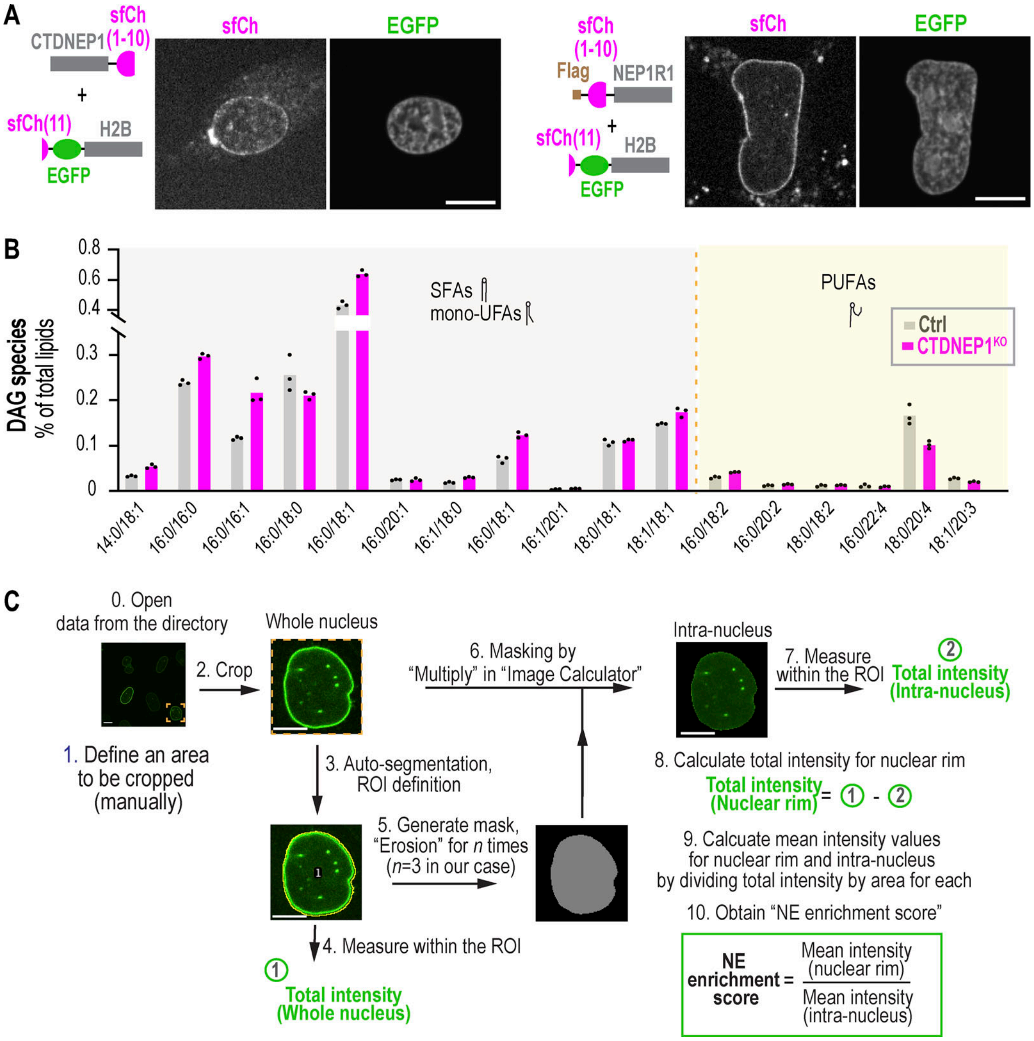

Figure S1. **CTDNEP1 can reach the INM, lipidomics analysis of DAG species in CTDNEP1 KO cells, and image analysis pipeline for NE enrichment score, related to Fig. 1. (A)** Spinning disk confocal images of live U2OS cells expressing indicated constructs. **(B)** Lipidomics analysis of DAG species in ctrl and CTDNEP1 KO U2OS cells. Plot of lipid species shows only those that were detected in all triplicate samples both from ctrl U2OS and CTDNEP1 KO cells, and thus the sum of the species in the plot is lower than the total levels of DAG. Each dot indicates a technical replicate. **(C)** Schematic representation of quantitation for NE enrichment score. All scale bars: 10 µm.

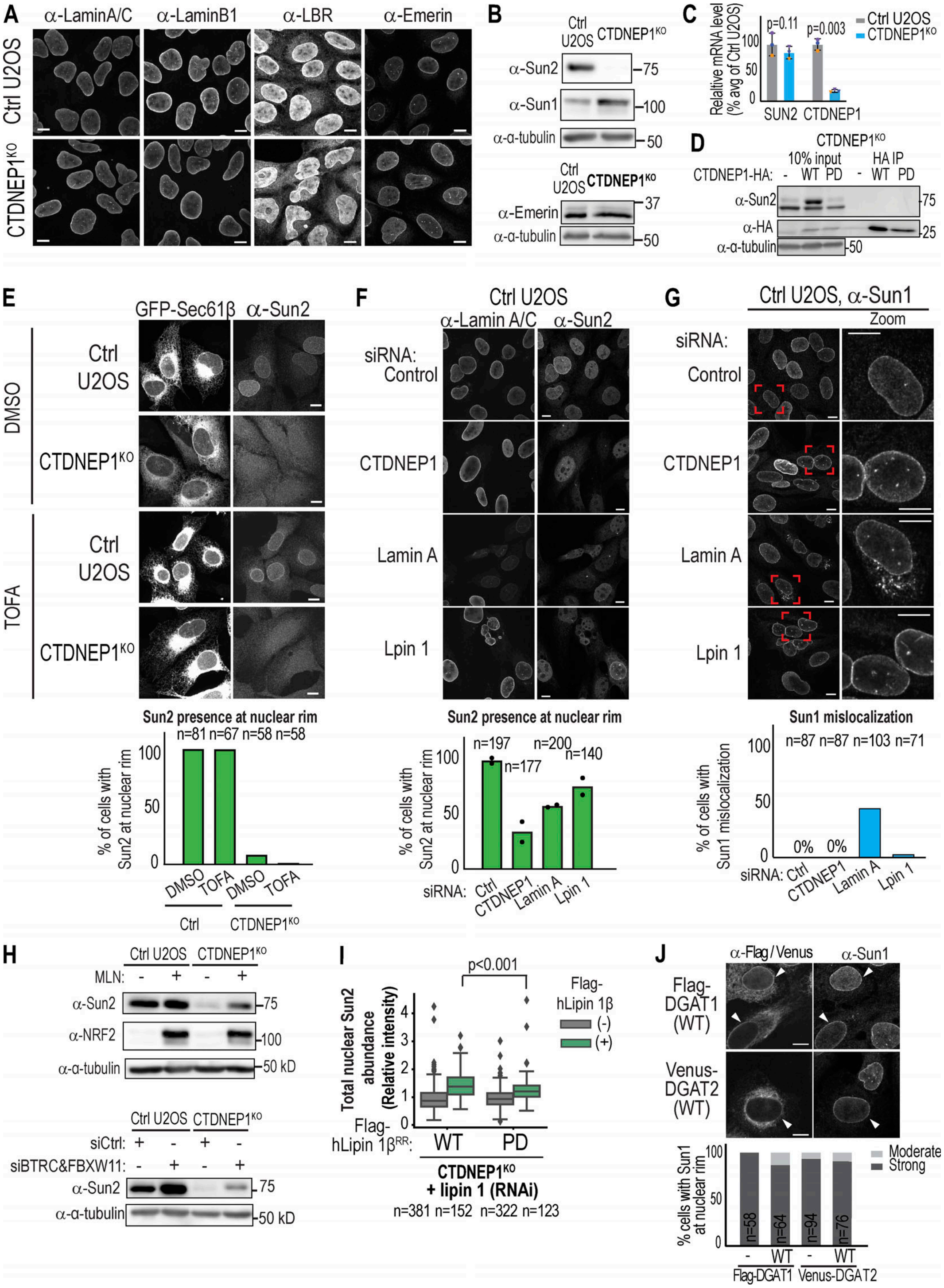

Figure S2. **Selective loss of Sun2 protein at the nuclear rim in CTDNEP1 KO cells is dependent on $\text{SCF}^{\text{bTRCP}}$ and DAG metabolism, related to Fig. 2.** **(A)** Immunofluorescence with indicated antibodies in U2OS cells. **(B)** Immunoblot of lysates from U2OS cells with indicated antibodies. **(C)** qRT-PCR of indicated cell lines for indicated genes, shown as fold change in expression relative to mean control values. *n* = 3 biological replicates (mean and SD). Each pair of replicates is color-coded. P values: paired *t* test. **(D)** Immunoprecipitation using anti-HA antibodies of lysates from CTDNEP1 KO cells without (−) or with stable expression of indicated constructs. **(E)** Max projected spinning disk confocal images and plot representing categorization of Sun2 localization at nuclear rim in indicated cell lines transiently expressing GFP-Sec61β and treated with TOFA. **(F and G)** Immunofluorescence with indicated antibodies in control U2OS cells treated with indicated siRNAs and plots representing categorization Sun2 or Sun1 at the nuclear rim. For G: boxed regions are magnified in the right column. **(H)** Immunoblot of lysates from U2OS cells with indicated antibodies and treatments. MLN is MLN4924; siRNA against BTRC and FBXW11 was used to RNAi-deplete $\text{SCF}^{\text{b-trcp}}$. **(I)** Boxplot representing automated fluorescence intensity quantification of Sun2 in the nuclear area (see Materials and methods) under indicated conditions. Data were pooled from two independent experiments. P values: Tukey HSD test. **(J)** Immunofluorescence of control U2OS cells transiently expressing indicated constructs. Plot represents blind categorization of Sun1 localization at nuclear rim. Scale bars, 10 µm. In E–G, I, and J, *n* indicates the number of cells that were quantified. Source data are available for this figure: SourceData FS2.

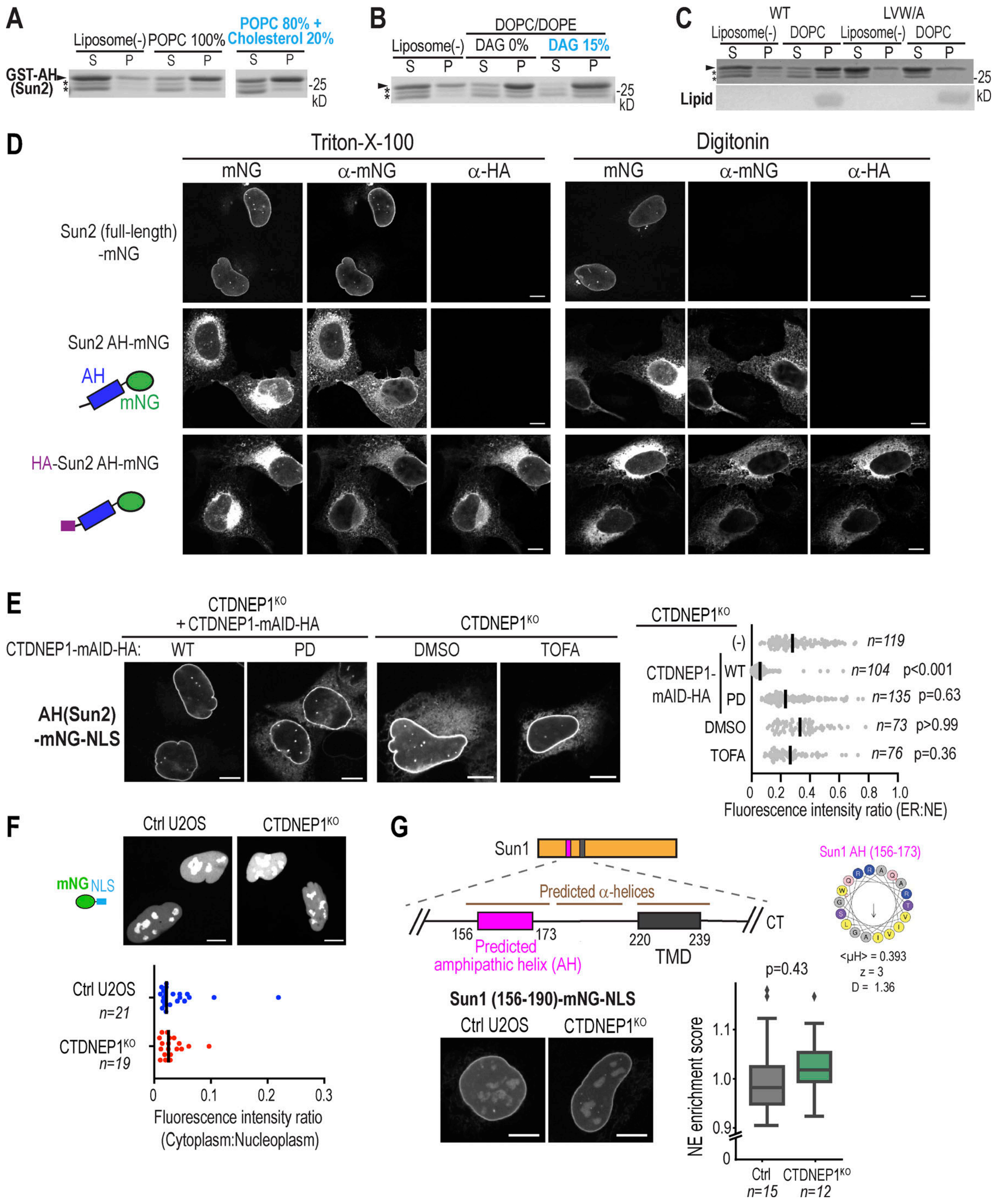

Figure S3. **Characterization of the AH of Sun2 in vitro and in vivo as a membrane associated protein segment that targets the INM when fused to an NLS in control U2OS cells and to the ER and INM in CTDNEP1 KO cells, unlike a predicted AH in Sun1, related to Fig. 3. (A–C)** Representative images of Coomassie stained gels of indicated in vitro purified proteins after liposome-cosedimentation assays with indicated lipid compositions. S, Soluble; P, Pellet. In A and B, WT GST-AH is shown; in C, WT and LVW/A AH mutant (top) and total lipids are shown (bottom). Arrowhead, GST-AH; asterisks, purification byproducts. **(D)** Spinning disk confocal images of U2OS cells immunostained with anti-mNG and anti-HA after permeabilization with indicated detergents. **(E)** Spinning disk confocal images of live CTDNEP1 KO cells expressing AH-mNG-NLS and transfected with CTDNEP1-mAID-HA WT or D67E (PD) mutant, or treated with TOFA. Plot represents quantification of ER:NE of mNG fluorescence intensity. P values (compared to [−]), Kruskal–Wallis test followed by Dunn's multiple comparisons test. **(F)** Spinning disk confocal images of live U2OS cells expressing mNG-NLS. Plot represents quantitation of cytosol:nucleoplasm ratio of mNG fluorescence intensity. **(G)** Schematic representation of N-terminal region of Sun1 highlighting predicted amphipathic helix (residues 156–173). Schematic of helical wheel projection generated by HeliQuest with hydrophobic moment <μH>, net charge z, and the discriminant factor D (right). Spinning disk confocal images of live U2OS cells transiently expressing Sun1(156-190)-mNG-NLS, and plot representing "NE enrichment score". P value: unpaired *t* test. Scale bars, 10 μm. In E–G, *n* indicates the number of cells that were quantified. In E and F, bar indicates median. Source data are available for this figure: SourceData FS3.

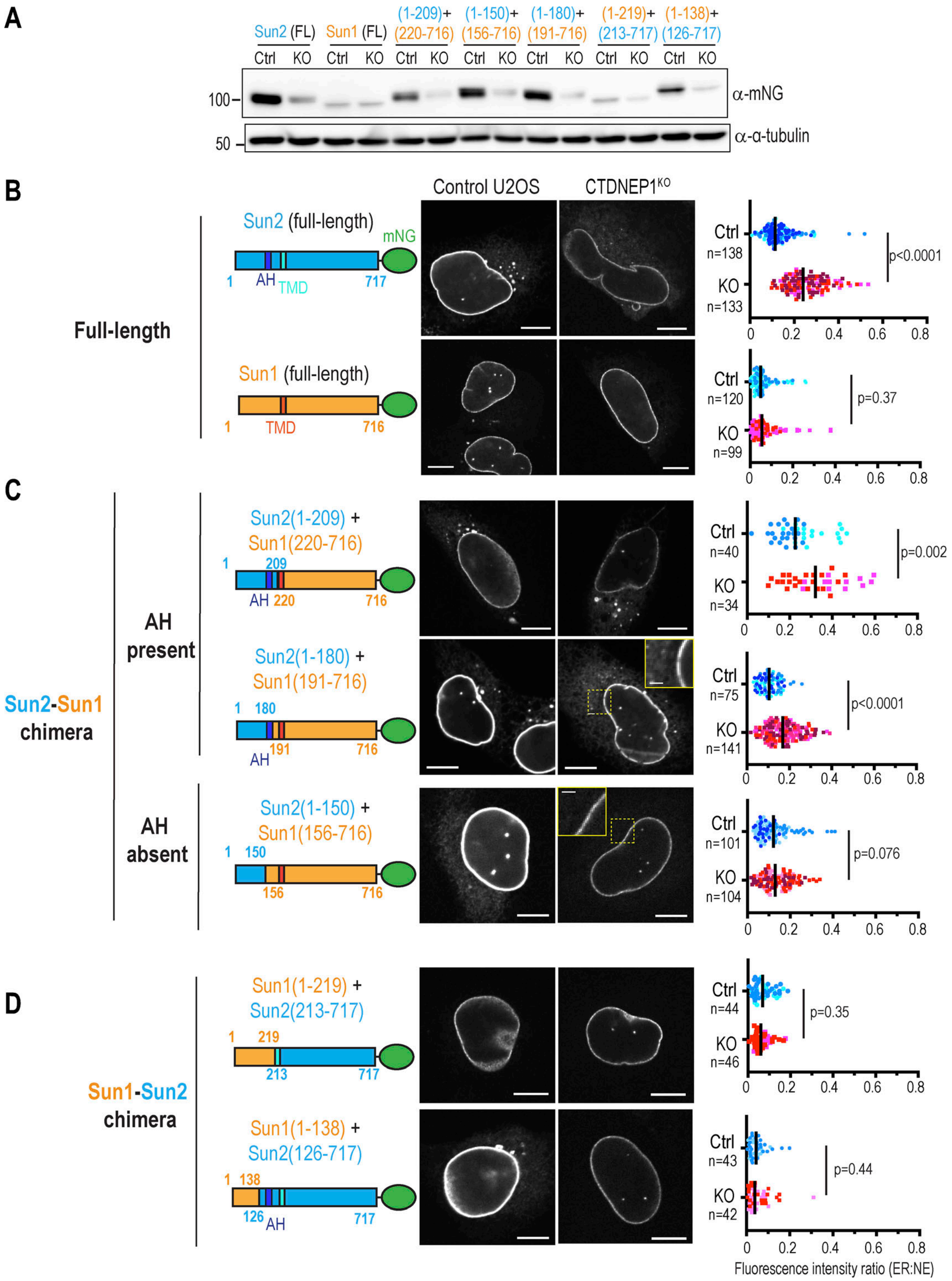

Figure S4. **Protein levels and localization of chimeric Sun2/Sun1 constructs, related to Fig. 3. (A)** Immunoblot of cell lysates transiently transfected with indicated chimeric constructs. **(B–D)** Left: Schematic representation of the Sun2/Sun1 full-length and chimera constructs. Numbers indicate amino-acid residue positions. Middle: Representative spinning disk confocal images of live cells transiently expressing indicated constructs. Scale bars, 10 and 2 µm (insets). Right: Plots representing the ER:NE mNG fluorescence intensity ratio. Dots are color-coded according to experimental replicates. Bar indicates median. P values: Welch's *t* test (for Sun2[1-180]-Sun1[191-716]) or unpaired *t* test (for others). *n* indicates the number of cells that were quantified. Source data are available for this figure: SourceData FS4.

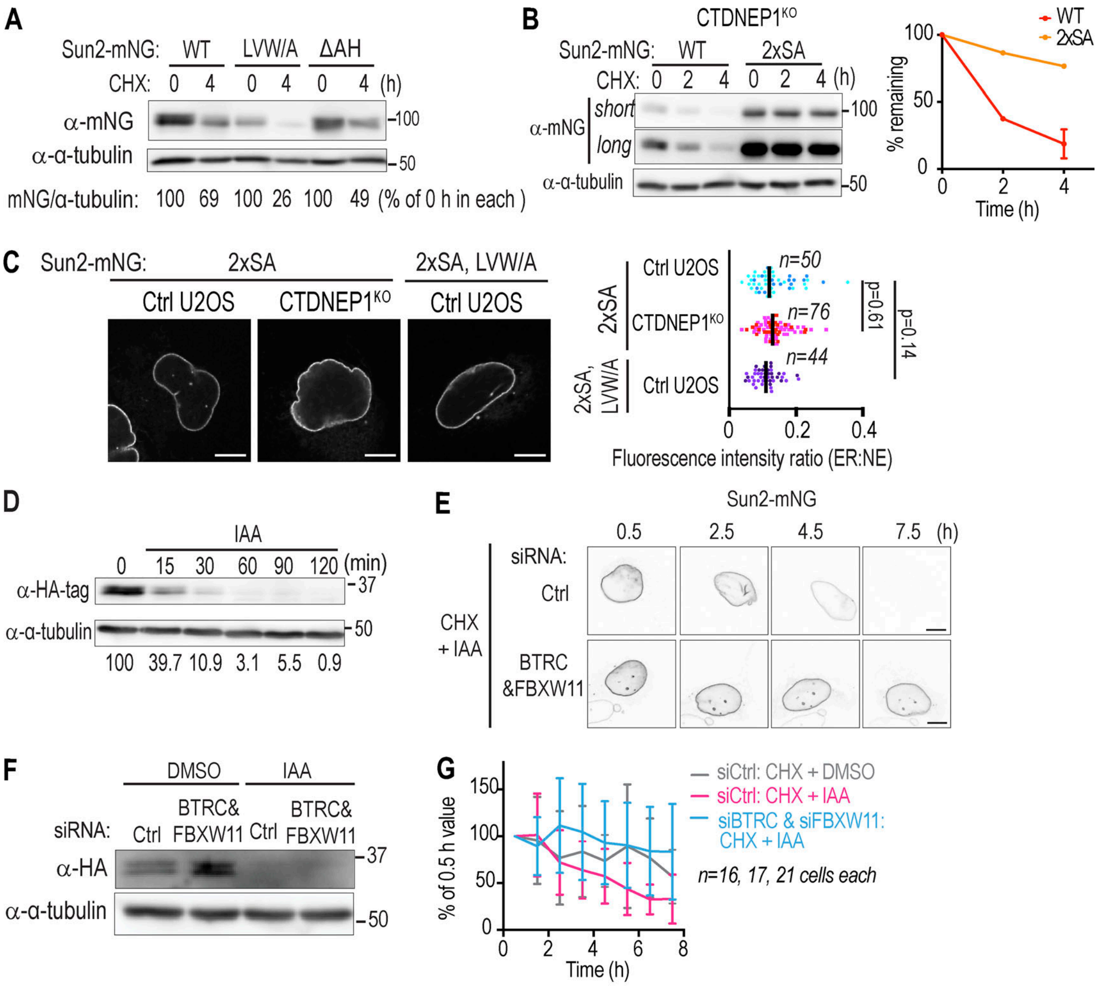

H

○: AH predicted ×: No AH predicted

Protein name	MemBrain	AmphipaSeeK
SUN domain-containing protein 1 (Sun1)	○	○
SUN domain-containing protein 2 (Sun2)	○	○
SUN domain-containing protein 5 (Sun5)	○	×
LEM domain-containing protein 2 (LEMD2)	○	○
Inner nuclear membrane protein Man1	○	×
Nuclear envelope integral membrane protein 1 (Nemp1)	○	×
Nuclear envelope integral membrane protein 2 (Nemp2)	○	○
Delta(14)-sterol reductase LBR	×	
Emerin	×	

Figure S5. **Mutation in the AH and serine rich regions of Sun2 affect its protein stability, dependence of Sun2 protein stability on SCF^{bTRCP} and presence of predicted AH sequences in other NE-associated proteins, related to Fig. 4. (A)** Immunoblot of cell lysates from ctrl U2OS cells transiently expressing indicated Sun2:mNG constructs following cycloheximide treatment (CHX) for indicated hours (h). **(B)** Immunoblot of cell lysates from CTDNEP1 KO cell line expressing indicated constructs treated with cycloheximide for indicated hours (h). Both short and long exposures are shown. Plots represent the intensity of bands from immunoblots as normalized to 0 h for each condition. WT are replicas of Fig. 3 K. *N* = 2 for all conditions (except *N* = 3 for wild type, 4 h) independent experiments. Mean (and SD where *N* = 3) shown. **(C)** Spinning disk confocal images of live U2OS cells expressing indicated Sun2-mNG constructs. Plots represent ER:NE ratio of mNG fluorescence intensity. Dots are color-coded according to experimental replicates. P values: Kruskal–Wallis test followed by Dunn's multiple comparisons test. *n* indicates the number of cells that were quantified. Bar indicates median. **(D)** Immunoblot of cell lysates from DLD-1 OsTIR-1 CTDNEP1(EN)-mAID-HA cell line treated as indicated. Values at the bottom show quantification of bands with antibodies against -HA-tag, normalized to bands with antibodies against α-tubulin and shown as % of 0 min. **(E)** Representative time-lapse images cells treated with CHX + IAA in Fig. 4 F. **(F)** Immunoblot of cell lysates from DLD-1 OsTIR-1 CTDNEP1(EN)-mAID-HA cell line treated with indicated siRNAs and then with IAA for 2 h. **(G)** Time-lapse confocal live images of DLD-1 OsTIR-1 CTDNEP1EN-mAID-HA cells transiently expressing Sun2-mNG, treated as indicated. mNG fluorescence intensity in ER region is shown as a percent of the value at 0.5 h (mean and SD). *n* indicates the number of cells that were quantified. Data were pooled from two independent experiments. **(H)** Table of presence of predicted AHs in human NE-associated proteins by MemBrain and AmphipaSeek. Scale bars, 10 µm. Source data are available for this figure: SourceData FS5.